SPE 110542

Fluid Flow in a Fractured Reservoir Using a Geomechanically-Constrained Fault Zone Damage Model for Reservoir Simulation

Pijush Paul, SPE, and Mark Zoback, SPE, Stanford University, and Peter Hennings, ConocoPhillips

This paper was prepared for presentation at the 2007 SPE Annual Technical Conference and Exhibition held in Anaheim, California, U.S.A., 11–14 November 2007.

Abstract

Secondary fractures and faults associated with larger, reservoir scale faults affect both permeability and permeability anisotropy and hence may play an important role in controlling the production behavior of a faulted reservoir. It is well known from geologic studies that there is a concentration of secondary fractures and faults in a damage zone adjacent to larger faults. Because there is usually inadequate data to incorporate damage zone fractures and faults into reservoir simulation models, in this study we utilize the principles of dynamic rupture propagation from earthquake seismology to predict the nature of fractured/damage zones associated with reservoir scale faults. We include geomechanical constraints in our reservoir model and propose a workflow to more routinely incorporate damage zones into reservoir simulation models. The model we propose calculates the extent of the damage zone along the fault plane by estimating the stress perturbation associated with dynamic rupture propagation. Fractures created by the stress pulse accompanying rupture propagation enhance permeability along reservoir scale faults in both the horizontal and vertical directions. We calibrate our modeling with observations from a number of studies and show that dynamic rupture propagation gives a reasonable first order approximation of damage zones in terms of permeability and permeability anisotropy in order to be incorporated into reservoir simulators.

Introduction

Fractures present both problems and opportunities for exploration and production from hydrocarbon reservoirs. The heterogeneity and complexity of fluid flow paths in fractured rocks always makes it difficult to predict how to optimally produce a fractured reservoir. It is usually not possible to define the geometry of the fractures and faults controlling flow and it is difficult to integrate data from markedly different scales associated with faults mapped in seismic surveys and those seen in wellbore image logs. A number of studies in hydrogeology and the petroleum industry have dealt with modeling fractured reservoirs.[1-4] Various methodologies, both deterministic and stochastic, have been developed to model reservoir heterogeneity on hydrocarbon flow and recovery. The work by Smart et al.[5], Oda[6-7], Maerten et al.[8], Bourne and Willemse[9], and Brown and Bruhn[10] quantify the stress sensitivity of fractured reservoirs. Several studies[11-13] that include fracture characterizations from wellbore images and fluid conductivity from the temperature and the production logs indicate fluid flow from critically stressed fractures. Additional studies emphasize the importance and challenges of coupling geomechanics in reservoir fluid flow.[14-16] These studies found that geomechanical effects may be very significant in some of the fractured reservoirs.

Secondary fractures and faults associated with larger scale faults appear to be quite important in controlling the permeability of some reservoirs. Densely concentrated secondary fractures and faults near larger faults are often referred to as damage zones, which are created at various stages of fault evolution: prior to faulting[17-19], during fault growth[20-25], and during the earthquake slip events[25-28] along the existing faults associated with rupture propagation.

Lockner et al.[29] and Vermilye and Scholz[23] show that the damage zones from the pre-faulting stage are very narrow and can be ignored for reservoir scale faults. The damage zone formed during fault growth can be modeled using dynamic rupture propagation along a fault plane[30-33].

In this paper, we first introduce a reservoir in which there appears to be significant permeability anisotropy associated with flow parallel to large reservoir scale faults. Next, we build a geomechanical model of the field and then discuss the relationship between fluid flow and geomechanics at well scale fracture and fault systems. To consider what happens in the reservoir at larger scale, we will utilize dynamic rupture modeling to theoretically predict the size and extent of damage zones associated with the reservoir scale faults. Finally, we utilize fine scale fluid flow simulations to illustrate the effects of these damage zones on permeability and permeability anisotropy of the reservoir. In contrast to static dislocation models due to slip events, which demonstrates the damage effects only at the tip of the existing faults, dynamic rupture propagation technique defines the damage zone all along the fault.

Field scale permeability anisotropy and project motivation

The chosen field area (CS) is located in the Timor gap between Australia and Indonesia. **Fig. 1** shows a structural map of the CS field, which has a number of large, reservoir scale faults striking in E-W direction. Seismic data show normal slip amounts as large as ~300m on some of these faults, some of which extend up to surface. Seismic data also show several small scale faults with N-S orientation. These faults have smaller slip and do not appear to extend to depths shallower than the reservoir. Regional tectonic studies indicate that the E-W oriented faults are strike-slip/normal faults. The reddish region in **Fig. 1** indicates the main reservoir, which is a horst structure in between two half-grabens. This map also shows locations of the exploratory wells (CSB1, CSB2, CSB3, CSB4, CSB5, CSU1, CSU2, CSU3, CSU4, CSF1, CST1 and CSH1), production wells (P1, P2, P3, P4, P5, P6, P7 and P8), and injection wells (I1, I2, I3 and I4) in the field. The exploration wells are all near vertical (the maximum deviation is ~5deg) while production and injection wells are deviated up to ~45deg.

Interference and tracer tests between injection and production wells show preferential flow along the reservoir scale faults trending in E-W direction (**Fig. 2**). The colored lines connecting wells in the figure indicate the relative permeability of the flow path between them. Red lines indicate the highest permeability paths and white and yellow lines indicate the lowest permeability paths. As shown in **Fig. 2**, lines sub-parallel to the large E-W trending fault colors are mostly red and pink, which indicate a relatively high permeability parallel to the faults. However, these same faults appear to be barriers to cross-fault flow and thus inhibit north-south flow within the reservoir. When we increase the permeability of blocks adjacent to the reservoir scale faults in the base simulation model, it shows an improvement in the production history match, suggesting a possibility of high permeability zone associated with these faults. We hypothesize that the enhanced flow parallel to the E-W trending faults but relatively low flow normal to them suggests that enhanced flow is occurring in the damage zones adjacent to these fault planes. Below, we propose a new technique for predicting the extent of damage zones for the purpose of incorporating them into reservoir simulation models in terms of their effect on localized permeability variations and large scale permeability anisotropy in the reservoir.

Petrophysical and Geomechanical model of the study area

Logs from the well CSU2 (**Fig. 3**) show that the reservoir section is separated in two parts by an unconformity. The upper section, *Formation-1,* is comprised largely of sandstone with alternate mudstone and siltstone beds. Sandstone layers show a coarsening upward profile and are occasionally bio-turbated. Mudstones contain modular pyrite and siderite nodules and are occasionally laminated and bio-turbated. The lower section, *Formation-2,* is composed predominantly of sandstone with alternate mudstone layers. Log response indicates sandstones as high energy deposit with occasional to no bio-turbation. Both the formations are from a fluvial-deltaic dominated depositional environment and have porosity of ~10-15%. These formations show cross-bedding, faulting and occasional natural fractures. Borehole images show very low fractures density in the exploratory wells. The reservoirs have mostly matrix dominated porosity and permeability. Average reservoir permeability is ~100-200mD but core and log measurements show permeability up to ~1200mD in places, which correlates with production logs and well tests from those intervals.

Dual caliper measurements and core samples from Formation-1 and 2 suggest that while the sandstones are fairly strong, fractures in the samples sometimes act as planes of weakness that decrease the strength. Triaxial and unconfined strength (UCS) measurements on core samples from well, CSU2, at Formation-1[34] are used to calibrate a log-derived rock strengths. Samples from MD 3065m and 3128m show an average UCS value of ~75MPa while samples from MD 3085m and 3092m, which are more shaly, show a relatively lower average value of ~65MPa. We represent the continuous rock strength for the sandstone intervals using the empirical UCS model proposed by McNally[35] using the core UCS values. For shaly intervals, we define the UCS by the power law using the dynamic Young's modulus as proposed by Castillo et al.[34]. However, because most of the wells do not have S-wave measurements, we also define the shaly-sand UCS with only P-wave slowness, which is done by normalizing the power law model proposed by Horsrud[36] with the core data from the shaly intervals. Continuous UCS values for both sand and shaly intervals along with core UCS values are shown in the right most column of **Fig. 3**.

We analyzed wellbore resistivity images and dual arm calipers to identify drilling-induced tensile fractures and breakouts within the reservoir section of the CS field. Analysis from all exploratory wells shows breakouts in approximately NW-SE orientation with ~30-70deg of breakout widths and tensile fractures in the orthogonal (NE-SW) direction, thus giving the orientation of present day S_{Hmax} (**Fig. 4**). This observation is consistent with the regional maximum horizontal stress orientation found by Castillo et al.[34]. S_{Hmax} orientation is quite similar at all of the well locations around the field but varies with depth near some of the well-scale faults and bed boundaries.

Following Zoback et al.[37] we use frictional faulting theory to constrain magnitudes of the horizontal principal stresses (S_{Hmax} and S_{hmin}) and the vertical stress (S_v) is estimated by integrating bulk density log at well locations. We find that in the reservoir section, S_v is ~72.2MPa at 3170m depth, and the overburden gradient is ~2.34SG (19.47ppg or 0.02277MPa/m).

Direct measurements of pore pressure in the reservoir section throughout the CS field indicate a hydrostatic pore pressure (P_p) gradient of ~1.04SG (8.66ppg or 0.01013MPa/m). Sonic log and other measurements do not indicate any overpressure zones in the section above the reservoir, so we assume a hydrostatic pore pressure for the entire section.

In situ least principal stress (S_3) is estimated using extended leak-off tests (XLOT), leak-off tests (LOT), and pressure while drilling (PWD) data. We analyze XLOTs measurements of well CSP2 at true vertical depths of 1926 m and 2971 m to estimate S_3. At ~1926m depth, XLOT shows a

fracture closure pressure of ~785psi (5.41MPa), which gives a S_3 gradient of ~1.65SG (13.7ppg or 0.01602MPa/m). At 2971 m depth, the fracture closure pressure is approximately ~2018psi (13.91 MPa), which gives S_3 gradient ~1.61SG (13.4ppg or 0.01567MPa/m). Pressure tests done on other parts of the field show similar S_3 gradients as illustrated in **Fig. 5**.

In the final step of the stress analysis, we estimate a magnitude of the maximum horizontal stress (S_{Hmax}) using the stress polygon technique proposed by Zoback et al.[37], where each stress polygon indicates the range of permissible stress magnitudes based on Coulomb frictional faulting theory. This technique uses the estimated values of S_V, UCS, S_{hmin}, P_p, and also wellbore failures as the guiding constrains. Other parameters required for the modeling are hole geometry, mud weight, sliding friction, Biot coefficient and Poisson's ratio. Breakout width, observed values of S_{Hmax} azimuth, and estimated UCS values give the range of S_{Hmax} magnitude. The presence of breakouts in Formation-1indicates that S_{Hmax} is higher than the UCS, ~72MPa, which gives a lower bound of S_{Hmax} gradient of ~2.52SG (21ppg or 0.02456MPa/m) in the sand intervals. After including the effect of shaly sand intervals and also the previously estimated S_{hmin} magnitude, we define the range of S_{Hmax} gradient as ~21±2ppg. Formation-2 breakouts are similar in nature to Formation-1 breakouts, so a reasonable approximation is to assume similar stress gradient for both formations.

Fig. 5 shows the principal stress magnitudes estimated from different parts of the field, indicating a strike-slip faulting regime. However, including the stress state in shaly sections or weaker sections, which shows some tendency of normal faulting, gives a strike-slip/normal faulting environment ($S_{Hmax} \geq S_v > S_{hmin}$) at reservoir depths, which is consistent with the geological history of the field area.

Fracture analysis at well scale

In this section, we analyze the geometry of the fractures from the wellbore resistivity images and correlate their flow properties using production logs and well test data. Image logs show sets of bedding planes in the sandstone formations, and drilling enhanced fractures and laminations in the shaly layers. Natural fractures are not prominent in any of the eight exploratory wells of the field. The possible reasons for low fracture density in the image logs are: 1) actual fracture density is very low, 2) fractures have high dip angle and probability of mapping a high angle fracture using an image log of a vertical well is very low, and 3) the image quality in some wells is poor.

The fractures that we observe at wells are generally associated with faults and bed boundaries. Rotation of the stress orientation associated with these fractured zones indicates shearing of some fractures during the drilling process. Among all exploratory wells, well CSU2 shows a relatively large fractured/damage zone in the reservoir section, which may be considered as the best zone to effectively represent fluid flow properties through the well scale faults and fractures. **Fig. 6** (right column) shows the wellbore resistivity image of the fracture zone from well CSU2. The red curve is a possible well scale fault, which separates high angle fractures from low angle fractures. Fractures are generally southerly dipping. The left column of **Fig. 6** indicates rotation in S_{Hmax} orientation just above the fractured zone.

Fluid flow through the well scale fractured zone

We analyze production logs from the reservoir section of the wells to estimate the contribution of the fractured zone in the fluid production. Next, we correlate well test analysis and core permeability to quantify the effect of fracture porosity and permeability in the reservoir flow model. **Fig. 7** shows the production logs, spinner and gradiometer (column 3), and temperature logs (column 4) with the petrophysical model (column 1) and the fractures (column 2) from the same zone shown in **Fig. 6**. In column 5 of **Fig. 7**, we can see core permeability of the fracture zone. Both spinner and temperature logs indicate that most of the fluid enters into the well through intervals 3103-3104.5m, 3105.5-3109m, and 3120-3124m. These intervals are relatively clean sands with negligible clays. However, fractures are mainly concentrated at interval 3110-3114m, which is a relatively shaly section and do not show significant contribution in the fluid production. Core measurements indicate a permeability at the order of ~800-1200mD for high producing intervals and ~200mD from the fractured interval. The petrophysical explanations for the low fluid production from the fractured interval are the presence of clay in the fractured zone and high matrix permeability in the adjacent zones, which may mask the effect of fractures within the entire test zone.

To find if fractures are contributing to fluid flow away from the well, we also analyzed the well test data from the same interval. Pressure transient analysis of the well test data does not support dual porosity and dual permeability behavior in the reservoir, which again verifies a relatively negligible effect of fractures on the fluid flow. Constraining the well test model with the kH (where k is the permeability from core measurements and H is the thickness of zones using the production logs) ratio of high producing intervals and the rest of the well test interval shows that a dual layered well test model fits best with the observed pressure transient data (**Fig. 8**). In **Fig. 8**, we see first (green) and second (red) derivatives of observed pressure values with incremental time (x-axis). Continuous red and white curves on the top of first and second derivative points are the response of the best fit dual layer model, which has the skin of the higher permeability layer (s1) = -3.31, skin of the low permeability layer (s2) = -3.06, kH ratio (κ) = 0.88, storativity ratio (ω) = 0.21, and transmissivity ratio (λ) = 3.75×10^{-7}. The estimated permeability from the well test model for individual layer is close to the core permeability. Also, the thickness ratio between high and low production zones is reproduced as the storativity ratio by the well test model. Thus, the results from this exercise are consistent with the production data analysis shown in **Fig. 7**, which shows that the fluid flow pattern at well scale is stratigraphically controlled and the effect of fluid flow through fractures is possibly masked due to high matrix permeability of the reservoir.

Effect of stress on fluid flow

The laboratory experiments done by Makurat et al.[38] and Olsson et al.[39], show change in transmissivity due to shear dilation and normal closure on the fractures. For a fracture system with a multitude of fractures with different direction and geometry, the actual transmissivities or the changes in transmissivities of the critically oriented fractures are much higher than the respective parameters of the other fractures[11, 40]. Critical orientation is the orientation of fractures/faults in which the shear-normal stress ratio on them is sufficient to produce a shear failure.

To test if the relatively low fluid production from the fractures of the well CSU2 may also be related to its geometry in the current stress field, we analyze these fractures with respect to the estimated stress and pressure profiles. **Fig. 9** illustrates the value of Coulomb Failure Function (CFF) on a stereonet (lower hemisphere projection) and classifies the fractures as critically and non-critically stressed fractures. Fracture and faults (shown as poles) in higher CFF range (red color area) are optimally oriented for shear failure in the given stress state. A 3D Mohr diagram indicates the fractures with respect to the frictional failure line. Fractures above the frictional failure line are critically stressed and should add extra permeability to the reservoir matrix permeability. However, we see that only a few fractures from the well CSU2 are optimally oriented for shear failure in the given stress field, which may be one of the explanations why these fractures do not show significant contribution in fluid production comparing to the high permeability matrix sections.

Fracture density vs. the distance from reservoir scale faults

In the above sections, we see that the well scale fractures/faults do not show significant contribution in fluid production of a reservoir with high matrix permeability. However, interference tests done between various production and injection wells in the field show preferential flow along the large reservoir scale faults. In this section, we study the relationship between fracture densities at exploratory well locations versus their distance from the reservoir scale faults. First, we plot the number of fractures observed in the reservoir section of all exploratory wells with respect to the MD ~TVD (exploratory wells are almost vertical) of points where wells intersect the fractures. We find that the fracture swarms are correlated with the well scale faults or bed boundaries, and for most of the cases they coincide with the rotation in stress orientation. Then, to find a relationship between fracture density and reservoir scale faults, we derive the best fit lines on fracture versus depth distribution, ignoring the localized fracture swarms. The plot of the slopes of these lines with respect to the distance from the reservoir scale faults (**Fig. 10**) indicates that the fracture density decreases with the distance from the reservoir scale fault. A logarithmic best fit line gives the quantitative relationship (Eq. 1) between the parameters.

$$f_{md} = -0.294\ln(d) + 2.3612 \quad (1)$$

where f_{md} is number of fractures/MD and d is distance from the reservoir scale fault in meters. Eq. 1 gives a fracture density value of around 2 fractures/m at a distance close to the reservoir scale faults, which is an order higher than fracture density away (>1000m) from the faults. However, most of the exploration wells are far from the reservoir scale faults. The closest exploration well (CSB1) is ~200m away from the fault, which is very common in the oil industry. The small number of fractures in some wells and the limited numbers of wells suggest using this relationship with extreme caution. Thus, to estimate the fracture density in the damage zones associated with the fault, we propose to use geomechnically-constrained models using dynamic rupture propagation techniques.

Damage zone modeling using the dynamic rupture propagation technique

What traces do faults leave behind during their evolution? In field observations and laboratory measurements, we see that the displacement on the fault plane is maximum near the center and it tapers off to zero at the edges. When slip accumulates in the interior of the faults, stress concentrations at the fault tips also increases and the fault has to grow in its dimension to relax those stresses. During this process, faults develop a highly cracked zone around the tip, which is called a process zone. These are a dominant part of the damage zone when a fault becomes mature with time. From field observations, as shown in **Fig. 11**, we see that the width of the process zone increases linearly with the fault length. If we interpret the process zone as a dominant part of the damage zone, then the damage zone formed due to stress concentrations at the tip of the propagating fault should show a similar scaling law. However, this linear scaling relationship fails to include the effects of other dimensions of the fault. Also, if we use the static elastic crack model to predict the effects of damage zone then the parameters required are virtually impossible to estimate for all events during fault growth. Hence, we use the propagation of a dynamic rupture front along the fault plane to model the dimension of the damage zone.

During an earthquake, rupture starts on a small patch and propagates along the fault plane with time. Stress concentrations at the tip of the rupture front give the dimension of process zone, which may be scaled to the damage zone that is created during the fault growth. Rupture events originating in different orientations and from different patches may explain the multiple fracture patterns associated with the damage zones. These fracture patterns control the permeability anisotropy of the damage zone. The geometry and size of the damage zone controls the large scale permeability anisotropy in the reservoir. In this study, we combine the analytical solutions of dynamic rupture propagation by Freund[41] and Madariaga[30] to define the creation of a damage zone due to the stress perturbations at the rupture front.

In the dynamic rupture propagation technique, the source which creates the earthquake is assumed to be a dynamically extending planar crack. The pre-existing fault provides a weak path for the growth of the crack. Because confining pressure reduces the effects of tensile stresses near the crack tip, the crack extends along the fault plane, which might otherwise

lead to an oblique crack growth. The medium is considered to be an isotropic elastic material. The elastodynamic stress and deformation fields define the dynamic stress intensity factor and the dynamic energy release for the crack propagation. Particle velocity near the crack tip defines the stress perturbations due to a dynamic crack.

The elastodynamic solution of dynamic rupture propagation proposed by Freund[41] needs an on-plane solution of shear stresses at the rupture front. If we assume that the dynamic crack initiates as a self-similar circular-shear-crack then the solution proposed by Madariaga[30] gives an on-plane solution of shear stress at crack tip. A self-similar shear crack starts from a point and then grows symmetrically with a constant rupture velocity without stopping, until it suddenly stops at a time, leaving a final rupture front radius. When the rupture radius grows sufficiently large so that dynamic stress intensity factor for on-plane shear becomes greater than dynamic stress intensity factor for anti-plane shear, rupture front becomes elliptical with major axis sub-parallel to anti-plane direction because rupture prefers to grow in that direction.

For a dynamic crack, the speed of crack propagation or rupture velocity guides the spatial distribution of the crack. When rupture velocity becomes zero, the expression solves for a stationary crack. This solution for spatial distribution of a dynamic crack is independent of the configuration of the body and the details of how the system has been loaded, but it depends on the spatial position of the crack tip with time.

We have seen above that by combining the on-plane solution of a dynamic circular crack[30] to Freund's[41] solution we can estimate stress tensors around the rupture front. Using the stress values with respect to the rock strength we can estimate the extent and nature of the damage or fractured zone, which can be used in a reservoir simulation model. However, to estimate higher order variations in the damage zone width, we have to numerically simulate the rupture front propagation of a dynamic crack originating as an arbitrary shape.

In the next section, we discuss a workflow and the parameters required to estimate damage zone width using the dynamic rupture propagation technique.

Methodology and input parameters

In this section, we discuss the methodology to estimate the damage zone width using a reservoir scale fault from the CS field. We also discuss the assumptions related to rupture source location and the stress perturbation and the nature of failure due to rupture propagation along an exiting fault.

The structural model of the study area indicates that the major faults in the reservoir strike sub-parallel to the E-W direction. The average dip of the E-W striking faults is ~45º with a maximum value of ~60º. The N-S striking faults have an average dip of ~60º and the maximum dip is ~78º. As discussed before, some of the E-W striking faults show throw as high as ~300m. The N-S striking faults show maximum throw of ~60m. Large cumulative throws along the faults indicate that these faults must have slipped several times in the geological past.

To determine whether the throw observed in the seismic data may have occurred under the present day stress conditions or in a geological stress condition, we study the reservoir scale faults with respect to the present day stress field. **Fig. 9** illustrates the Coulomb Failure Function (CFF) at present day stress state for a set of well scale fractures. The red zones in the figure indicating features with strike E30ºN to E5ºS or NS to N30ºE, and dip greater than 60º are the favorable geometries for slip in the present day stress conditions. This suggests that even though the E-W striking faults have favorable strike direction they may not slip in the present day stress condition because their dip angle is too shallow (<60º). However, some of the N-S striking faults have strike and dip both optimally oriented for a shear failure. Because the E-W striking faults show larger throw than the N-S striking faults in the seismic data, the E-W faults likely slipped in a historical stress regime.

To estimate the historical stress state when the E-W reservoir scale faults likely slipped, we first find all possible stress states which could result in slip on the faults with the given geometries. Then we constrain the magnitude and orientation of the stresses using the stratigraphic/geological history of the area. The geological history and the nature of slip observed through the seismic interpretations indicate a normal faulting or a dominant dip-slip regime when the E-W striking faults slipped in the past. Stratigraphic studies indicate that the reservoirs were at a shallow depth (~2/3 of the current reservoir depth of ~3500m) when most of the slip occurred in the E-W striking faults. Based on this information we estimate a historical lithostatic gradient ~13ppg or 0.0152MPa/m, which defines the vertical stress, S_v. S_v is also the maximum principal stress in a normal faulting environment. The minimum principal stress or the minimum horizontal stress, S_{hmin}, is sub-parallel to the dip direction of the E-W striking faults and the maximum horizontal stress, S_{Hmax}, is sub-parallel to the strike direction. The S_{hmin} gradient is ~8.8ppg or 0.0104MPa/m and S_{Hmax} is ~10.52ppg or 0.0123MPa/m. A historical stress regime for the N-S striking fault is also a normal faulting environment with the slip along the dip, which gives the direction of S_{hmin} along the E-W direction. These faults may have been activated if S_{Hmax} at the time of the slip on the E-W striking faults is relaxed to a level lower than the S_{hmin} such that the horizontal stresses switched orientations. The magnitudes of the stresses when the N-S trending faults may have slipped are estimated to be: S_v ~13ppg or 0.0152MPa/m, S_{Hmax} ~8.8ppg or 0.0104MPa/m, and S_{hmin} ~8.7ppg or 0.0106MPa/m. For both E-W and N-S striking faults, the pore pressure, P_p, is ~5.8ppg or 0.0068MPa/m. These estimations are based on stratigraphic evidence, but they are a source of uncertainty in determining the damage zone modeling. In the next section, we discuss how to incorporate the uncertainties of the input parameters in modeling the damage zone using the dynamic rupture technique.

The other input parameters that are required to estimate damage zone width in the dynamic rupture propagation technique are the velocity profiles (P-wave, S-wave, and rupture velocities), the rock strength, and the stress drop during slip. First, we define the P-wave velocity using a power law of the confining pressure (Eq. 2). The P-wave velocity is calibrated against the P-wave velocity from the sonic logs at the present day reservoir depth i.e. ~4500m/s at ~3500m.

$$\alpha = 55(P_{conf})^{1/4} \quad (2)$$

where α is the P-wave velocity in m/s, and P_{conf} is the confining pressure due to the overburden.

Then all other parameters except stress drop are correlated to the P-wave velocity. For this study, we use the S-wave velocity, β, as 0.55 of the P-wave velocity. Rupture velocity, v, is related to the S-wave velocity as a gradient from the deepest point on the faults to the shallowest point on the faults of the study area. The Uniaxial Compressive strength, UCS, is estimated from the P-wave slowness, Δt, as discussed in a previous section. Rock strength is related to the UCS, which is based on the triaxial measurements done on the core samples at reservoir depths. Again, to estimate the reservoir properties at the time of slip when the depth was ~2/3 of the current depth, all the above parameters are calculated using P_{conf} at ~(2/3)z. **Fig. 12a** and **12b** show the rupture velocity and rock strength profiles along the studied fault of the CS field. Because there is no earthquake data available, we assume the stress drop ~1MPa which is a typical value observed from a good size earthquake on faults of this size.

Next, we need a rupture source to model the effect of rupture propagation along a fault plane. For a reservoir that does not have any recorded earthquake data such as this study area, we can not identify the actual source points of the rupture initiation. For this study, we assume the bottom-center point of the fault as the source point for the rupture initiation (**Fig. 13**), which simulates a fault growing from bottom to top. The dynamic rupture starts from a source with a simple circular shape but gradually becomes elliptical because the dynamic stress intensity for an on-plane shear is larger than an anti-plane shear.

For the simplicity of calculation, we also assume that the global coordinate system at the source point is parallel to a local coordinate system at the rupture front, i.e. x-axis and z-axis are sub-parallel to the average strike and dip direction of the fault, and y-axis is perpendicular to the fault plane (**Fig. 14a**). This is a valid assumption because reservoir scale faults are generally planer on a first order approximation, and the rupture prefers to propagate along the weakest path, i.e. the fault plane.

Once we know the source point of the dynamic rupture and the input parameters to model its effects, we can use the combined solution of Freund[41] and Madariaga[30] to estimate the stress perturbations around the reservoir scale faults. **Fig. 14b, 14c** and **14d** illustrate the components of the stress tensor at the rupture front in the directions 90º, 45º, and 0º from the fault plane. Stress values are calculated at the reservoir depth (~3500m) of the fault shown in **Fig. 12**. We see that the shear component, s_{zy}, is the dominant component (larger than normal components) in all three cases, which creates high angle features in the damage zone. In the case along the fault (0º from z axis), s_{zy} is the largest component, and the s_{zz} and s_{zx} components are almost zero, which creates large failure features that strike sub-parallel to the parent fault. These large fault parallel features ahead of the rupture front help to propagate the rupture along the fault plane, or in an actual growing fault case, some of these failure planes coalesce and support growing the fault. In a direction perpendicular to the fault plane, the s_{zx} and s_{zz} components are larger in comparison to the 0º case, which reduces the size of the features. They strike in a direction slightly deviated from the strike of the parent fault. In the 0º case, the principal stresses are almost sub-parallel to the coordinate system with maximum compression sub-parallel to the parent fault and minimum compression perpendicular to the fault. For the 90º case, the principal components are of smaller magnitude and they are oriented in slightly different angle from the parent fault, which gives the failure features with higher dip angle than the 0º case, but features are smaller in size. **Fig. 15a** and **15b** show the schematic of the damage zone dimension and the nature of failure planes in cross section and map view respectively. Stress intensity increases towards the rupture front, which results in a higher fracture intensity.

In **Fig. 14**, we can see that without the rupture propagation effect, the far-field octahedral shear is lower than the rock strength so failures do not occur. During rupture propagation, the rupture front octahedral shear combines with the far-field octahedral shear and the total exceeds the rock strength, which creates a damage around the rupture front. The dimension of the damage zone is greatest in the 0º case (~78m) and gradually decreases to ~42m in a direction perpendicular to the fault plane. This gives an elliptical shape to the damage zone with the major axis along the fault.

In the damage zone of the studied fault, which is a normal fault by origin, dynamic rupture hypothesis gives normal faulting pattern for the secondary failure features. This is consistent with the field observations where we see secondary normal fault adjacent to a large normal faults. If the features in the damage zones are optimally oriented in the present day stress state, they give a preferential flow parallel to the strike of the parent fault. High angle failure planes increase the permeability in the vertical direction. But the change in permeability due to damage zone features perpendicular to the strike of the parent fault is less or negligible, particularly for a reservoir with high matrix permeability such as our study area. This is due to the strike of the secondary features being sub-parallel to the strike of the parent fault and the width of damage zone is limited in comparison to the block size of the upscaled model. Later in this paper, we discuss a fine scale simulation study to verify the effects of permeability anisotropy within the damage zone.

Uncertainty analysis

As discussed before, the input parameters and the stress values used to model the damage zone may include a lot of uncertainty. This section discusses how to incorporate the effects of those uncertainties in estimating the properties of the damage zone. This is done with Monte Carlo Simulation of each parameter at every estimation point. The Monte Carlo method uses pseudo-random numbers to incorporate the uncertainty around the best possible value of a parameter. In this study, the pseudo-random numbers are generated by a Gaussian algorithm, in which we assume the best possible value as the mean value and define a standard deviation around it to incorporate the range of uncertainty in the parameter.

We have already discussed the way to estimate the mean values of the parameters in the previous section. **Fig. 16** illustrates the uncertainty ranges of the input parameters and

the corresponding effects on the damage zone width at the reservoir depth (~3500m) of the same fault shown in **Fig. 12**. The analysis of 100 simulations indicates that stress drop is the most sensitive parameter in determining the width of the damage zone using the dynamic rupture technique. The histogram of the damage zone width shows a dominant uncertainty range of the damage zone width is between 20m to 60m with an average of ~45m; however, some values may go up to 120m.

Fig. 17a and **17b** shows the mean and standard deviations of damage zone width from all 100 simulations. At reservoir depths, the damage zone width is ~40-60m at the center of the fault and ~70-100m at the edges of the faults, which is consistent with the field observation of the damage zone width for the faults of this length (**Fig. 11**). The standard deviation or uncertainty range of the damage zone width is on the order of ~5m to 20m at the reservoir depth but higher in places where the estimated damage zone width is larger.

To verify the dynamic rupture technique further, next we discuss the damage zone modeling of the Nojima fault where we know the width of the damage zone through the scientific boreholes drilled through the fault, and also have a better idea of the rupture source on the fault.

Damage zone modeling of the Nojima Fault

In this study, we model the damage zones using the rupture propagated during the Kobe earthquake (1996) of M 6.9 in the Nojima fault and compare them with core observations from the scientific boreholes. The Nojima fault runs along the northwestern margin of the Awaji Island of Japan. This fault is a right-lateral active fault with a minor reverse slip component. It trends in NE-SW direction (average strike ~N40°E) and dips in SE direction at a high angle (~80°). It juxtaposes granitic and grano-diorite rocks and partly overlain by the sediments of different geological ages.[42-43] The dimension and properties of the Nojima fault for this study is based on the study done by Wald[44]. **Fig. 18** shows a schematic of the slip distribution found by Wald[44] and the location of the rupture source. Rupture fronts are elliptical in shape with the major axis sub-parallel along the dip of the fault. Because the Nojima fault is a strike slip fault and rupture front prefers to travel in anti-plane direction (along the dip) rather than on-plane direction (along the strike). The UCS, around the Nojima fault is defined using a normalized UCS model proposed by Hickman and Zoback[45] for the granites around the San Andreas Fault. This model uses P-wave velocity to estimate UCS.

We model the 100 equally-likely cases of the damage zone width using the dynamic rupture technique. **Fig. 19a** and **19b** illustrates the mean and standard deviation of those simulations. The mean values of the damage zone width decrease width the increase in the depth. At the intersection points of the GSJ borehole (~625m) and NIED borehole (~1150m, ~1320m, ~1800m) with the Nojima fault, the estimated damage zone widths are ~44m, ~37m, ~33m, and ~23m respectively. At these intervals, the standard deviation values of the damage zone width from all simulations indicate a range of 3.5-7.0m with higher range towards the shallower sections. **Fig. 20** shows that the estimated damage zone widths are consistent with the damage zone width observed in the core samples from the boreholes by Lockner et al.[46]. Permeability measurements in the core samples from these intersecting zones indicate a 4-5 higher order magnitude in damage zone with respect to the intact rock. As the Nojima fault damage zone modeling study also verifies that the dynamic rupture technique gives a reasonable first order approximation of the damage zone width, next we discuss the results of damage zone modeling for all the reservoir scale faults of the CS field.

Damage zone width for the faults from the CS field

In this section, we discuss the damage zone modeling results for all the faults of the CS field using the dynamic rupture propagation technique. The input parameters are already discussed in a section before. We use same input parameters for both E-W and N-S trending faults except they have different stress regime to generate rupture on them.

Fig. 21a and **21b** show the mean and standard deviation from the 100 simulations for all the E-W trending faults. At the reservoir depth, the average damage zone width from all faults varies from ~60m (center of the fault) to ~140m (edges of the fault). However, we can see that most of the contributions in this average value come from the few large faults and smaller faults have relatively narrow damage zones. Standard deviation for those 100 simulations varies from ~15-40m with higher values correspond to higher damage zone width.

Fig. 22a and **22b** illustrate the mean and standard deviation from 100 simulations using a west side view for all N-S striking faults. In this case, the average damage zone width at reservoir depth is ~20m at center and ~60m at the edges, which is much smaller that the EW striking fault. This is because N-S striking faults are much smaller in size in comparison to E-W trending faults. The standard deviation in this case varies from ~7-18m.

As discussed before, interference and tracer tests between production and injection wells show high permeability anisotropy along the EW trending fault, which are consistent with the modeling results because larger damage zones width along E-W faults give better fluid flow path in comparison to smaller N-S trending faults. In the next section, we discuss a fine scale simulation study through damage zone to quantify the relative nature of permeability anisotropy in the reservoir due to the presence of damage zones.

Permeability anisotropy due to the damage zone

We quantify the permeability anisotropy effect due to the damage zone using a fine scale simulation study. The size of the model is 360x380x14m^3, which is the average block size of the reservoir simulation model of the CS field (**Fig. 23**). Failure planes in the damage zone are created using the stochastic technique in the places where the dynamic rupture technique gives the possibility of shear failure. Then they are defined as discrete features in the model. As shown in **Fig. 23**, failure planes are mostly striking parallel to of the south face of the block, which is the fault face in the upscaled reservoir model. We can also see that fracture density decreases away from this fault face of the model and becomes zero beyond the limit of the damage zone.

Using the discrete fracture model we generate a fine scale unstructured grid with total cells ~900,000. **Fig. 24b** represents the simulation grid, where we can see smaller tetrahedrons in the damage zone defining the discrete fractures. **Fig. 24a** shows a model of same size but without damage zone fractures. We define the matrix porosity as 0.13 and permeability (k_m) as 150mD. Fracture permeability is defined as 10^5 times k_m. One face of the model along the flow are defined as injector with 500bbl/day of water injection and opposite face is defined as producer with production at pressure constraint equivalent to reservoir pressure, 4000psi. Running the simulation for a single phase flow till both the injector and producer face reach at steady state gives the pressure difference (ΔP) between the two faces of the model. Now if we compare the simulations for the cases with and without fractures using the same fluid, the pressure difference (ΔP) and the flow rate inside the models (Eq. 3) give the change in the permeability along the flow due to the presence of fractures.

$$\frac{K_2^*}{K_1^*} = \frac{\Delta P_1 . Q_2}{\Delta P_2 . Q_1} \qquad (3)$$

where K^*_1 and K^*_2 are the equivalent or upscaled permeability along the flow for the models without and with fracture. ΔP_1 and ΔP_2 represent the pressure difference, and Q_1 and Q_2 represent the flow rate inside the model for without and with fracture cases for a steady state solution.

To define the permeability anisotropy due to the fractures in the damage zone, we repeat the experiment for flow along all the three possible principal flow direction of the model. In our experiment, we find that the permeability sub-parallel to the reservoir scale fault increases by ~2.6 times due to the presence of the damage zone. In the vertical direction, permeability increment is ~2.2 times but across the damage zone there is a slight decrease in permeability, ~0.97 times the matrix permeability. Because these are hypothetical experiments, the values of permeability enhancement can be only used as the trend of permeability anisotropy due to the damage zone, which is high along the reservoir scale faults and also in the vertical direction. This anisotropy effect is more enhanced in case of high contrast between the matrix and fracture permeability. Also, it is relatively more visible for a low matrix permeability than a high matrix permeability case, which is consistent with the production and well test analysis in our study area, where the effects of fractures at well scale are masked due to high matrix permeability.

Conclusions

In this paper, we present a workflow to estimate the damage zone associated with reservoir scale faults using dynamic rupture propagation. We find that the damage zone width gradually increases with the increase of the distance from the origin point of the rupture. At the reservoir depth of the CS field, we find a damage zone width of ~50-140m for the E-W trending faults and ~20-60m for the N-S trending faults, which are reasonable values and consistent with the field observations. The dip and strike of failure planes are parallel to the parent fault ahead of the rupture front but are slightly deviated away from the fault. Fine scale simulation studies indicate an increase in permeability along the strike of the fault and in the vertical direction due to this effect, which are consistent with the preferential flow orientation indicated by the interference and tracer tests in the CS field.

By implementing the effects of fractures associated with the reservoir scale faults to a simulation model, we can quantify the permeability anisotropy in the reservoir due to damage zones and can improve production predictability. In this paper, we use analytical solutions to model damage zones, which gives a reasonable first order approximation. However, numerical modeling techniques using the same concepts will be needed for accurate results in a complex and dynamic environment.

Future work will include optimal upscaling techniques to implement the effects of the damage zone in a reservoir simulation model and also to verify their effects with history matching of the production data.

Acknowledgments

We thank ConocoPhillips Co. for providing the data for this investigation. We also want to thank the Stanford Rock Physics and Borehole Geophysics consortium for funding this project. We want to acknowledge Dr. Mohammad Karimi-Fard and Dr. Bin Gong from the department of Energy Resource Engineering, Stanford University and Dr. Tapan Mukerji from the department of Geophysics, Stanford University for their useful advice during various parts of the project.

References

1. Martel, S.J., and Peterson, J.: *"Interdisciplinary characterization of fracture systems at the US/BK site, Grimesl Laboratory, Switzerland", Int. J. of Rock Mech. and Min. Sc. Abstracts* (1991) **28**, 259-323.
2. Lee, S.H., Lough, M. F., and Jensen, C.L.: *"Hierarchical modeling of flow in naturally fractured formations with multiple length scales", Water Resources Research* (2001) **37**, 443-455.
3. Long, J. C. S., and Billaux, D. M.: *"From field data to Fracture Network modeling: An example incorporating spatial structure", Water Resources Research* (1987) **23**, 1201-1216.
4. Gringarten, E.: *"3-D geometric description of fractured reservoirs", Mathematical geology* (1996) **28**, 881-893.
5. Smart, B.G.D., Somerville, J.M., Edlman, K., and Jones, C.: *"Stress sensitivity of fractured reservoirs", Journal of Petroleum Science and Engineering* (2001) **29**, 29-37.
6. Oda, M.: *"Permeability tensor for discontinuous rock masses", Geotechnique* (1985) **35**, 483-495.
7. Oda, M.: *"An equivalent continuum model for coupled stress and fluid flow analysis in joined rock masses", Water Resour. Res.* (1986) **22**, 1845-1856.
8. Maerten, L., Gillespie, P., and Pollard, D.D.: *"Effects of local stress perturbation on secondary fault development", Journal of structural Geology* (2002) **24**, 145-153.
9. Bourne, S.J., and Willemse, E.J.M.: *"Elastic stress control on the pattern of tensile fracturing around a small fault network at Nash Point, UK", Journal of Structural Geology* (2001) **23**, 1753-1770.
10. Brown, S.R., and Bruhn, R.L.: *"Fluid permeability of deformable fracture networks", Journal of Geophysical Research* (1998) **103(B2)**, 2489-2500.

11. Barton, C. A., Zoback, M. D., and Moos, D.: *"Fluid flow along potentially active faults in crystalline rock", Geology* (1995) **23**, 683-686.
12. Townend, J., and Zoback, M.D.: *"How faulting keeps the crust strong", Geology* (2000) **28**, 399-402.
13. Wiprut, D., and Zoback, M.D.: *"Fault reactivation and fluid flow along a previously dormant normal fault in the northern North Sea", Geology* (2000) **28**, 595-598.
14. Chen, H., and Teufel, W.: *"Coupling fluid-flow and Geomechanics in Dual-porosity modeling of naturally fractured reservoirs – Model description and comparison", SPE 59043* (2003).
15. Couples, G.D., Lewis, H., Reynolds, M.A., Pickup, G.E., and Ma, J.: *"Upscaling fluid-flow and Geomechanical properties in coupled matrix+fracture+fluid systems", SPE 79696* (2003).
16. Bourne, S.J., Brauckmann, F., Rijkels, L., Stephenson, B.J., Weber, A., and Willemse, E.J.M.: *"Predictive modeling of naturally fractured reservoirs using geomechanics and flow simulation", ADIPEC0911* (2000).
17. Aydin, A., Johnson, A.M.: *"Development of faults as zones of deformation bands and as slip surfaces in sandstone", Pure and Applied Geophysics* (1978) **116**, 931-942.
18. Lyakhovsky, V., Ben-Zion, Y., Agnon, A.: *"Distributed damage, faulting and friction", Journal of Geophysical Research* (1997) **102**, 27635-27649.
19. Nanjo, K. Z., Turcotte, D. L., and Shcherbakov, R.: *"A model of damage mechanics for the deformation of the continental crust", Journal of Geophysical Research* (2005) **110**, doi: 10. 1029/2004JB003438.
20. Chinnery, M. A.: *Secondary faulting; Part 1. "Theoretical aspects; Part 2, Geological aspects", Canadian Journal of Earth Sciences* (1966) **3**, 163-190.
21. Cowie, P. A., and Scholz, C. H.: *"Physical explanation for the displacement-length relationship of faults using a post-yield fracture mechanics model", Journal of Structural Geology* (1992) **14**, 1133-1148.
22. Anders, M. H., and Wiltschko, D. V.: *"Microfracturing, paleostress and the growth of faults", Journal of Structural Geology* (1994) **16**, 795-815.
23. Vermilye, J. M., and Scholz, C. H.:*"The process zone; a microstructural view of fault growth", Journal of Geophysical Research* (1998) **103**, 12223-12237.
24. Pollard, D. D., and Segall, P.: *"Theoretical displacements and stresses near fractures in rock; with applications to faults, joints, veins, dikes, and solution surfaces". Atkinson, B. K., (Ed.), Fracture Mechanics of Rock, Academic Press, London* (1987), 277-349.
25. Reches, Z., and Lockner, D. A.: *"The nucleation and growth of faults in brittle rocks", Journal of Geophysical Research* (1994) **99**, 18159-18174.
26. Freund, R.: *"Kinematics of transform and transcurrent faults", Tectonophysics* (1974) **21**, 93-134.
27. Suppe, J.: *"Principles of Structural Geology", Prentice-Hall, New Jersey* (1985), 537.
28. Chester, F. M., and Logan, J. M.: *"Implications from mechanical properties of brittle faults from observations of the Punchbowl fault zone, California", Pure and Applied Geophysics* (1986) **124**, 79-106.
29. Lockner, D.A., Byerlee, J.D., Kuksenko, V., Pnonomarev, A., and Sidorin, A.: *"Observations of quasi-static fault growth from acoustic emissions, Fault mechanics and transport properties of rocks", international Geophysics Series, Academic Press, san Diego, CA* (1992) **51**, 3-31,.
30. Madariaga, R.: *"Dynamics of an expanding circular fault", Bulletin of Seismological Society of America* (1976) **66**, 639-666.
31. Kostov, B. V.: *"Selfsimilar problems of propagation of shear cracks", J. Appl. Math. Mech.* (1964) **28**, 1077-1087.
32. Virieux, J., and Madariaga, R.: *"Dynamic faulting studied by finite difference method", Bull. of the Seis. So. of America* (1982) **72**, 345-369.
33. Harris, R. A., and Day, S. M.: *"Effects of a low-velocity zone in a dynamic rupture", Bull. Seismol. Soc. Am.* (1997) **87**, 167-1280.
34. Castillo, D. A., Hills, R. R., Asquith, K., and Fischer, M.: *"Frictional and wellbore failure constraints for estimating the in-situ stress tensor in deep boreholes: Application to the Timor sea and Fault-seal integrity: The Sedimentary basins of Western Australia", Proceedings of the Petroleum Exploration Society of Australia Symposium, Perth* (1999), 1-20.
35. McNally, G. H.: *"Estimation of core measures rock strength using sonic and neutron logs", Geoexploration* (1987) **24**, 381-395.
36. Horsrud, P.: *"Estimating mechanical properties of shale from empirical correlations", SPE Drilling and Completion* (2001) **16(2)**, 68-73.
37. Zoback, M. D., Barton, C. A., Brudy, M., Castillo, D. A., Finkbeiner, T., Grollimund, B. R., Moos, D. B., Peska, P., Ward, C. D., and Wiprut, D. J.: *"Determination of stress orientation and magnitude in deep wells",Int. Journal of Rock Mechanics and Mining Sciences* (2003) **40**, 1049-1076.
38. Makurat, A., Barton, N., Rad, N.S., and Bandis. S.: *"Joint conductivity variation due to normal and shear deformation", Proc. Int. Symp. Rock Joints* (1990), 535-540.
39. Olsson, R., and Barton, N.: *"An improved model for hydro mechanical coupling during shearing of rock joints", Int. J Rock Mech Min Sci* (2001) **38(3)**, 317-329.
40. Barton, C.A., Hickman, S.H., Morin, R., Zoback, M.D., and Benoit, D.: *"Reservoir-scale fracture permeability in the Dixie valley, Nevada, geothermal field", Proceedings of Society of Petroleum Engineers/International Society of Rock Mechanics and Mining Sciences, SPE* (1998) **1-2**, 315-322.
41. Freund, L. B.: *"The Mechanics of dynamic shear crack propagation", Journal of Geophysical Research* (1979) **84**, 2199-2209.
42. Ando, M.: *Geological and geophysical studies of the Nojima fault from drilling", An outline of the Nojima fault zone probe, the Island arc* (2001) **10**, 206-214.
43. Tanaka, H., Fujimoto, K., Ohtani, T, and Ito, H.: *"Structural and chemical characterization of shear zones in the freshly activated Nojima fault, Awaji Island, southwest Japan", Journal of Geophysical Research* (2001) **106**, 8789-8810.
44. Wald, D. J.: *"Slip history of the 1995 Kobe, Japan, earthquake determined from strong motion, teleseismic, and geodetic data", Journal of Physics of the earth* (1996) **44**, 489-503.
45. Hickman, S. and Zoback, M. D.: *"Stress orientations and magnitudes in the SAFOD pilot hole", Geophys. Res. Lett.* (2004) **31**, L15S12, doi:10.1029/2004GL020043.
46. Lockner, D., Naka, H., Tanaka, H., Ito, H., and Ikeda, R.: *"Permeability and Strength of Core samples from the Nojima Fault of the 1995 Kobe Earthquake", Proc. of the Inter. workshop on the Nojima Fault Core and Borehole Data Analysis* (1999), 147-152.

SI Metric Conversion Factors

bbl	x	1.589 873	E-01 = m^3
ft	x	3.048*	E-01 = m
mD	x	10^{-15}	E-02 = m^2
psi	x	6.894 757	E-03 = MPa

* Conversion factor is exact.

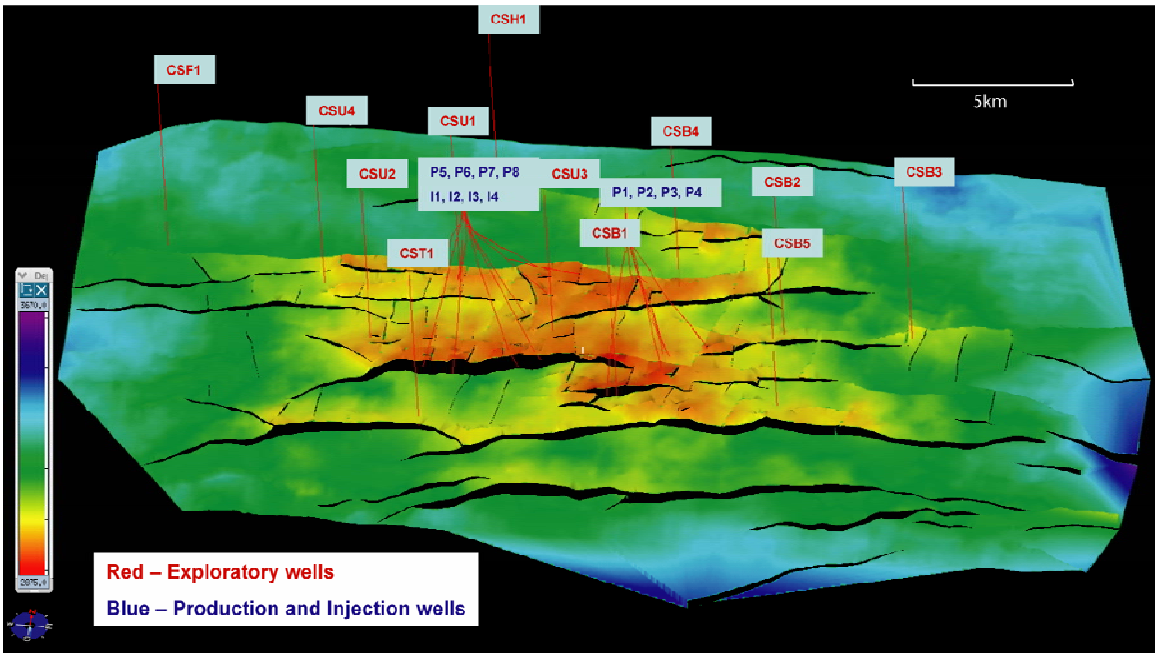

Fig. 1: Structural map of the CS field showing exploratory, production and injection well locations along with field scale faults. Red color indicates the highest points in the reservoir and blue color indicates the deepest points.

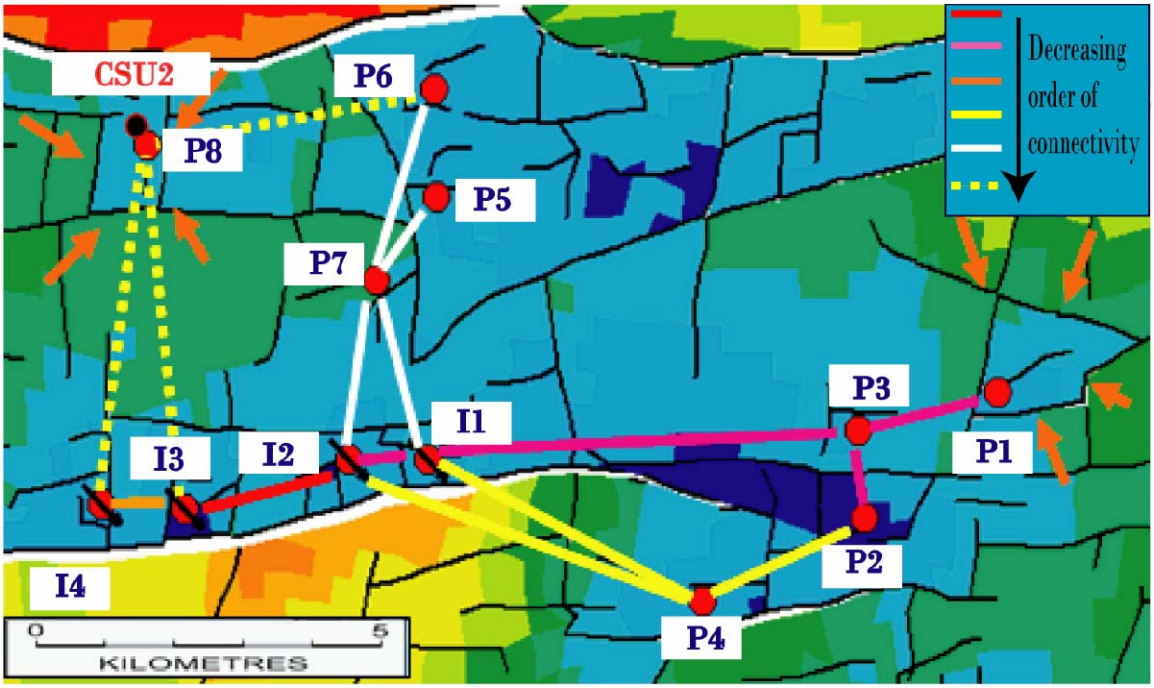

Fig. 2: Interference and tracer tests between injection (I1-I4) and production (P1-P8) wells show a high order of connectivity along the reservoir scale faults trending in EW direction. The lines connecting wells show relative permeability between the wells. The lines in red indicate the highest permeability paths and white and yellow lines indicate the lowest permeability paths.

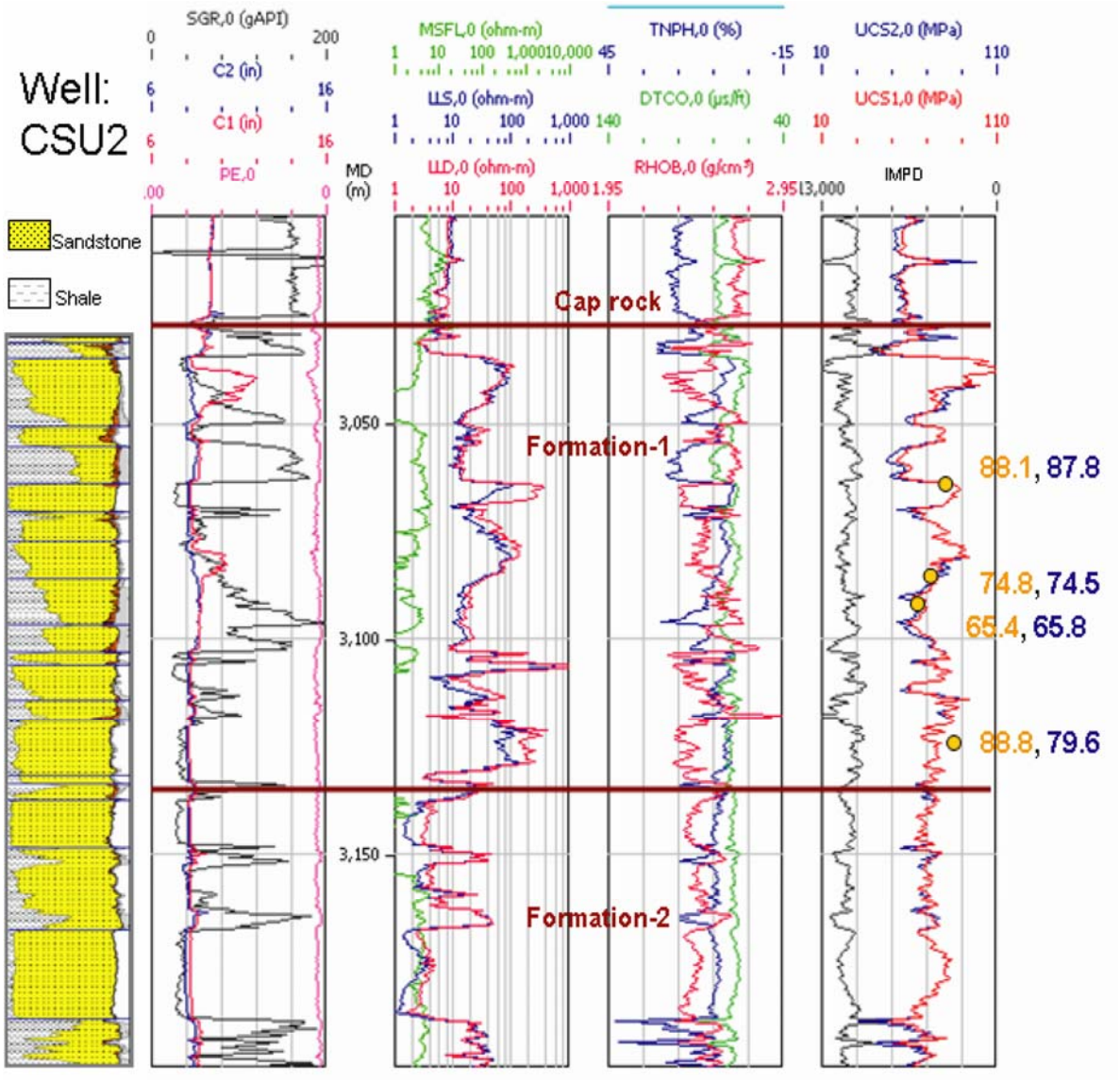

Fig. 3: Lithology encountered in well CSU2: Column1; SGR(Gamma Ray), C1(Caliper 1), C2 (caliper 2), PE (Photoelectric Factor): Column 2; Measured depth: Column 3; RHOB (Bulk Density), TNPH (Thermal Neutron Porosity), DTCO (Compressional Slowness): Column 4; LLD (Deep Resistivity), LLS (Shallow Resistivity), MSFL (Micro Shallow Resistivity): Column 5; Impedance, UCS1 (uses 'E' model-Equation 3 for shaly intervals), UCS2 (uses Δt model-Equation 4 for shaly intervals), Core UCS (dots): Column 6.

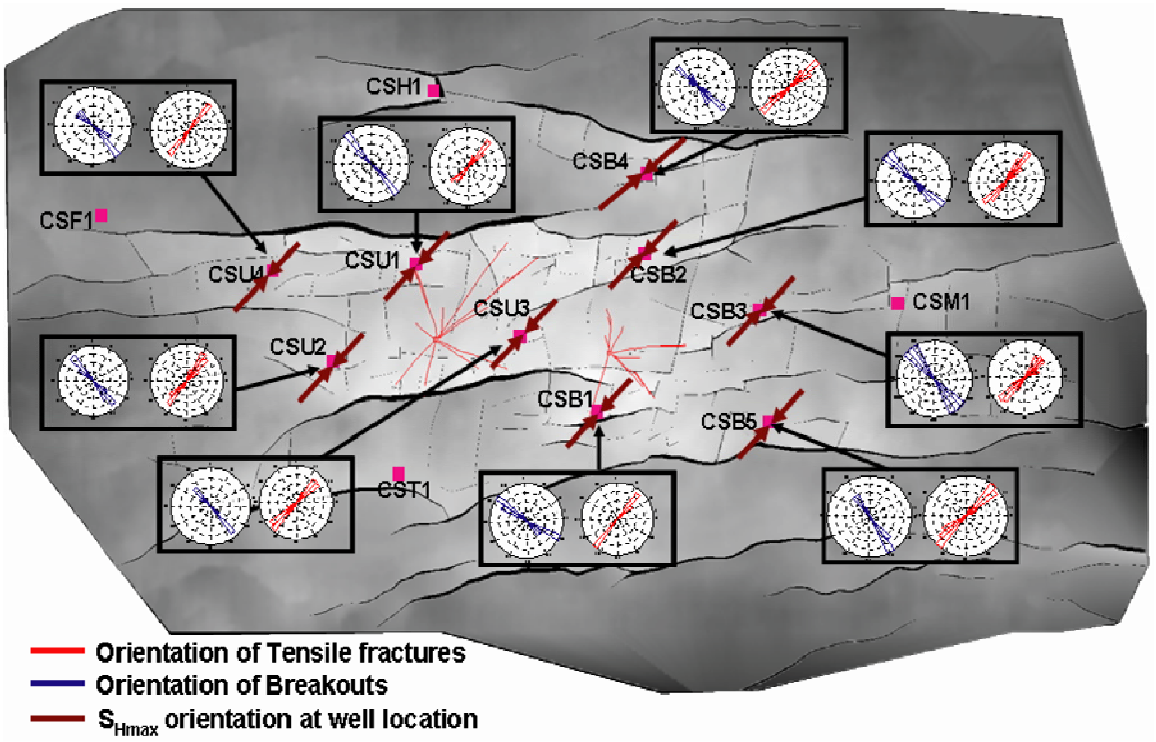

Fig. 4: Stress-induced wellbore breakouts and tensile wall fractures in the CS field consistently show a NE-SW direction of the maximum horizontal principal stress, S_{Hmax} . This direction is similar to the regional stress orientation as shown in the World Stress Map.

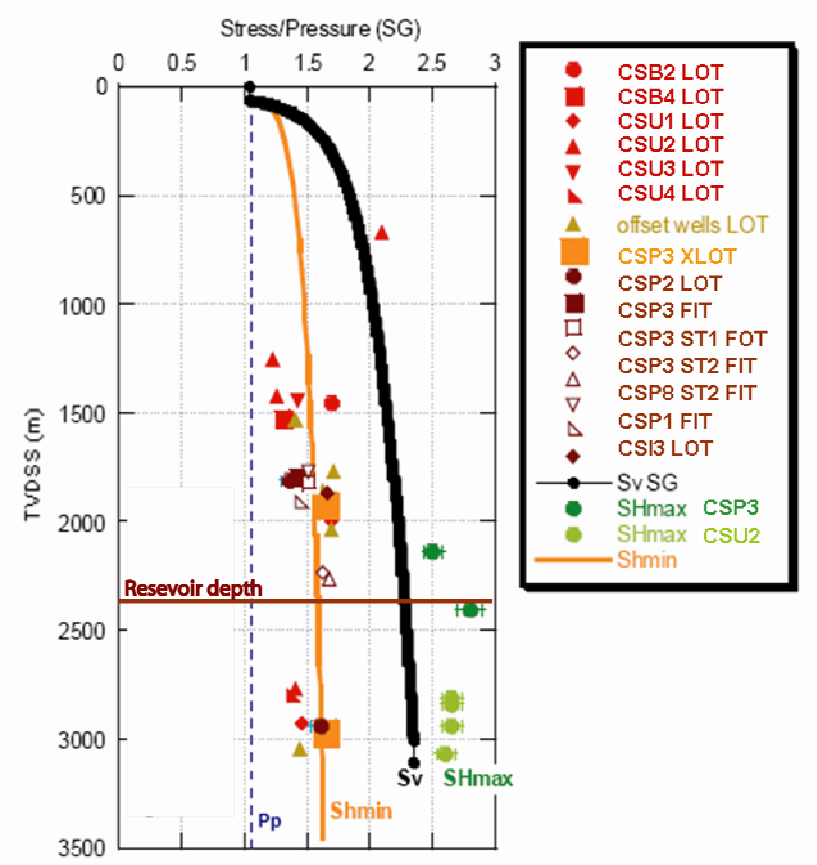

Fig. 5: Present day stress profiles (S_v gradient ~22.7 kPa/m, S_{Hmax} gradient ~24.5 kPa/m, and S_{hmin} ~15.6 kPa/m) and pore pressure profile (P_p ~10.1 kPa/m) at reservoir depth of the CS field. Note that the data indicate a Strike-Slip faulting regime.

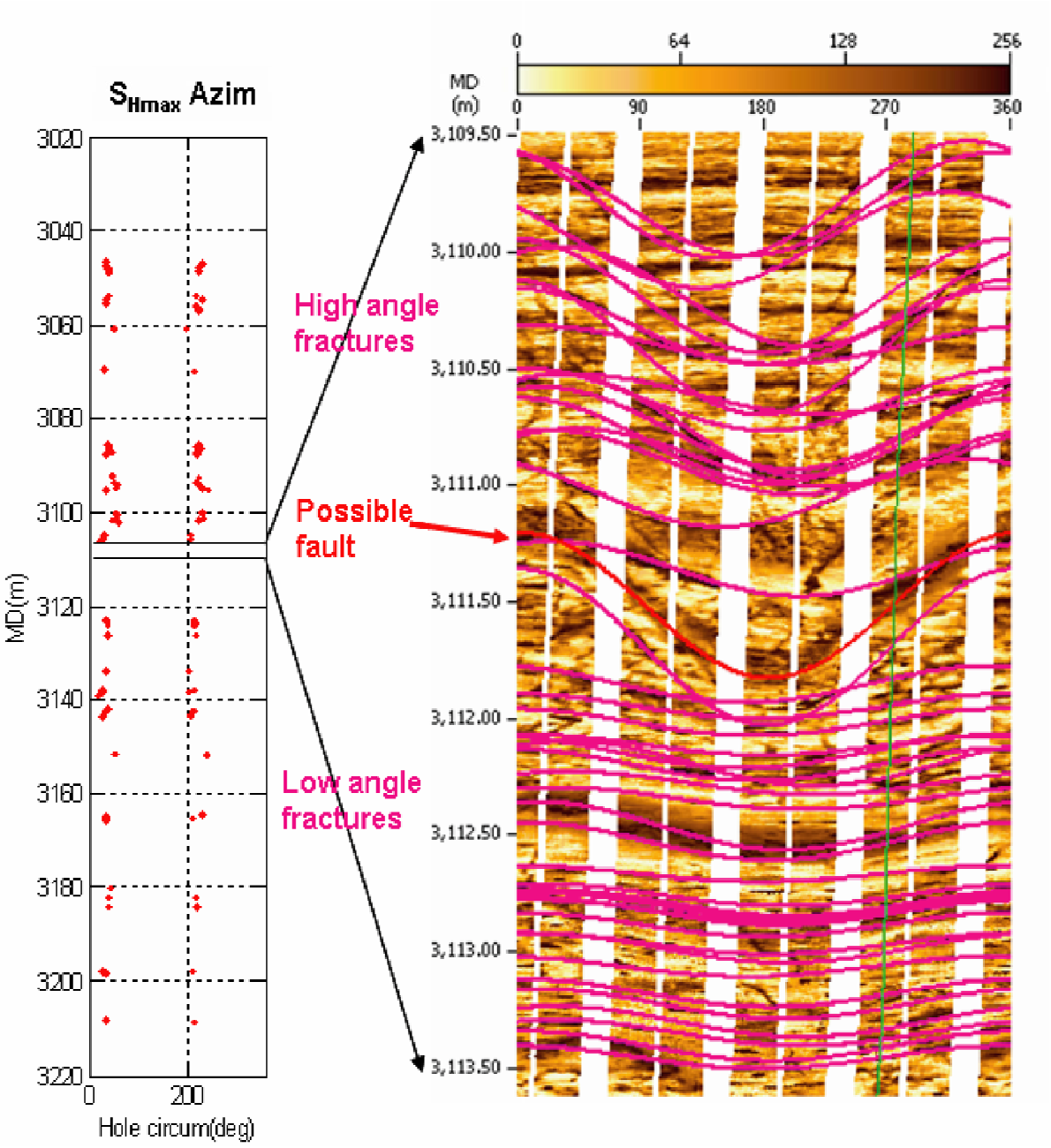

Fig. 6: The highest density fracture zone in well CSU2 shows that a small fault appears to separate high angle fractures from low angle fractures. A change in the observed S_{Hmax} orientation at the fault zone indicates that some of these fractures are active in the current stress field.

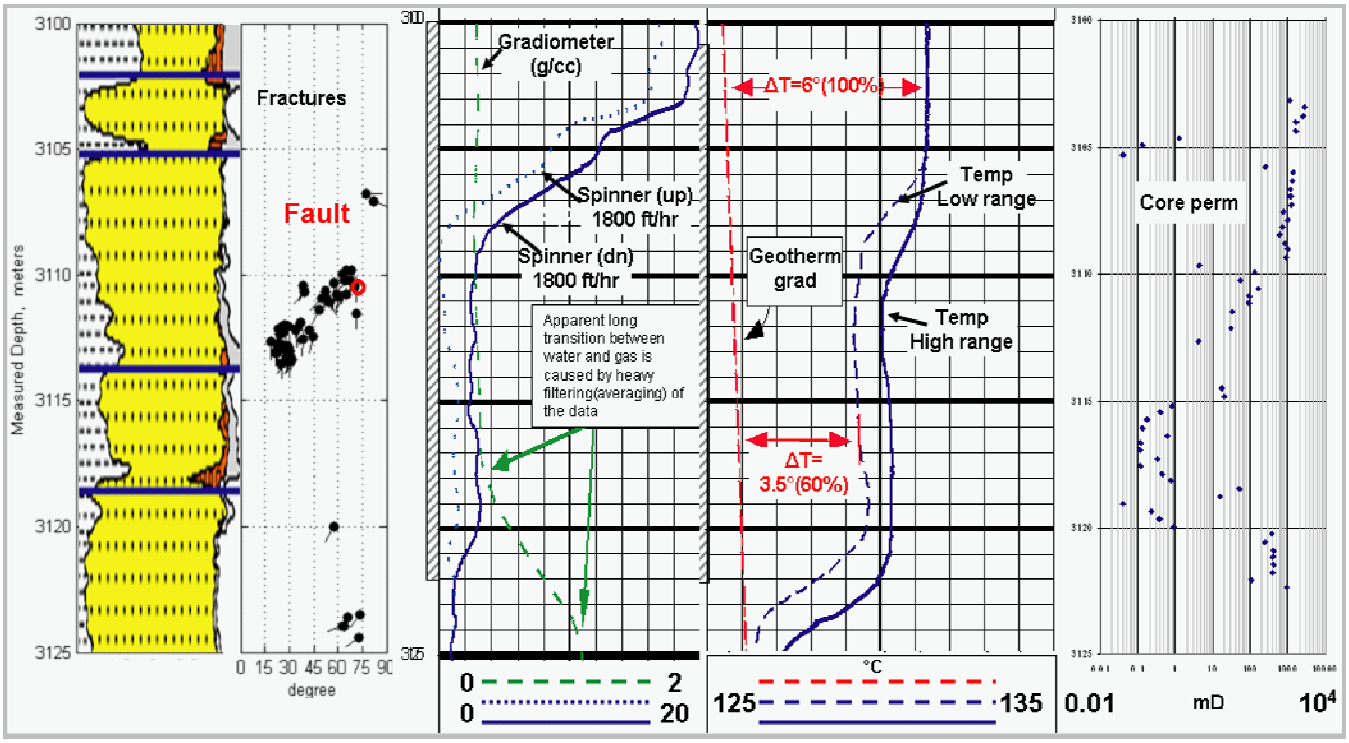

Fig. 7: In well CSU2, petrophysical model (column 1), fracture geometries as tadpoles (column 2), production logs, spinner and gradiometer (column 3), temperature logs (column 4), and core permeability (column 5) indicate that most of the fluid entering into the well through intervals 3103-3104.5m, 3105.5-3109m, and 3120-3124m. Fractures are mainly concentrated at interval 3110-3114m but this interval does not show any significant contribution in fluid production.

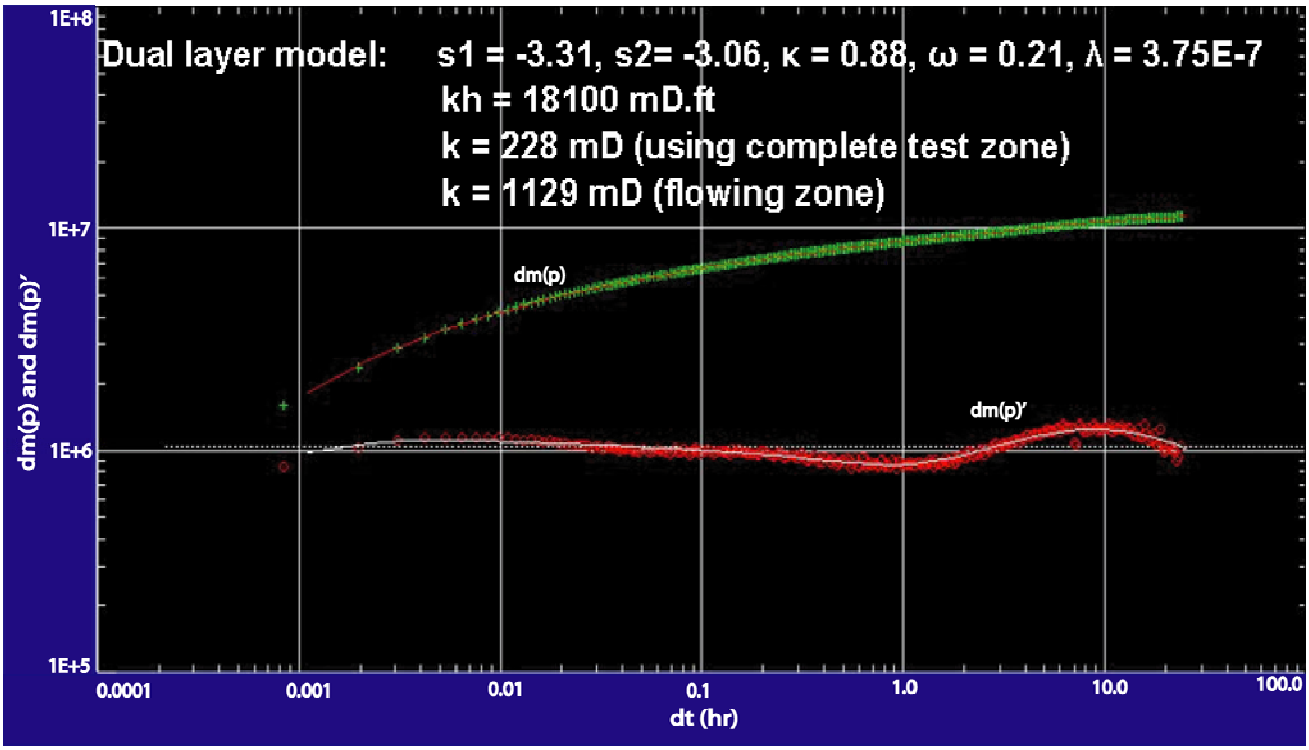

Fig. 8: In well CSU2, the dual layered well test model fits best with the observed pressure transient. The estimated permeability from the well test model is close to the core permeability and the thickness ratio between high and low production zones is reproduced as storativity ratio by a dual layer well test model but not by a dual porosity model, which again indicates relatively low production from the fracture system. S1 and S2 are the skin values of high and low permeable layers, λ = transmissivity ratio, ω = storativity ratio, and κ = kH ratio between high and low permeability layers.

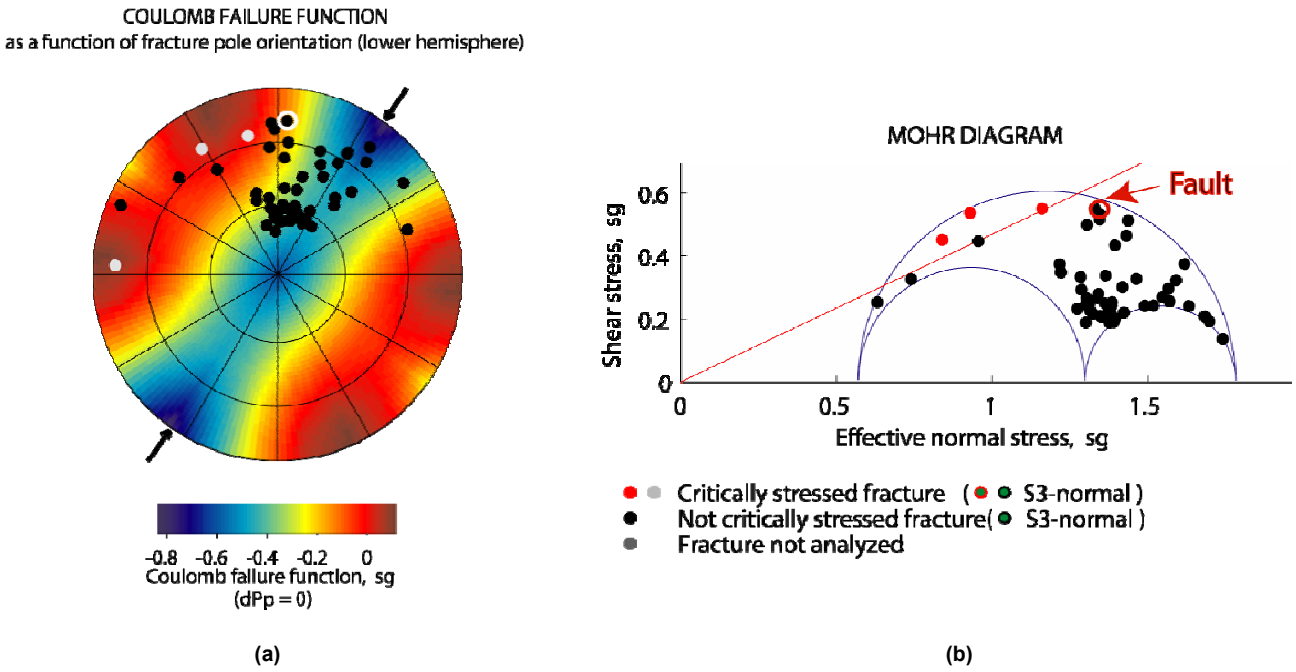

(a) (b)

Fig. 9: In well CSU2, (a) the stereoplot showing CFF in a lower hemisphere projection indicates optimally oriented zones (dark red color). (b) A 3D Mohr diagram with frictional coefficient line of 0.5 indicates that only a few fractures are in a frictional failure state.

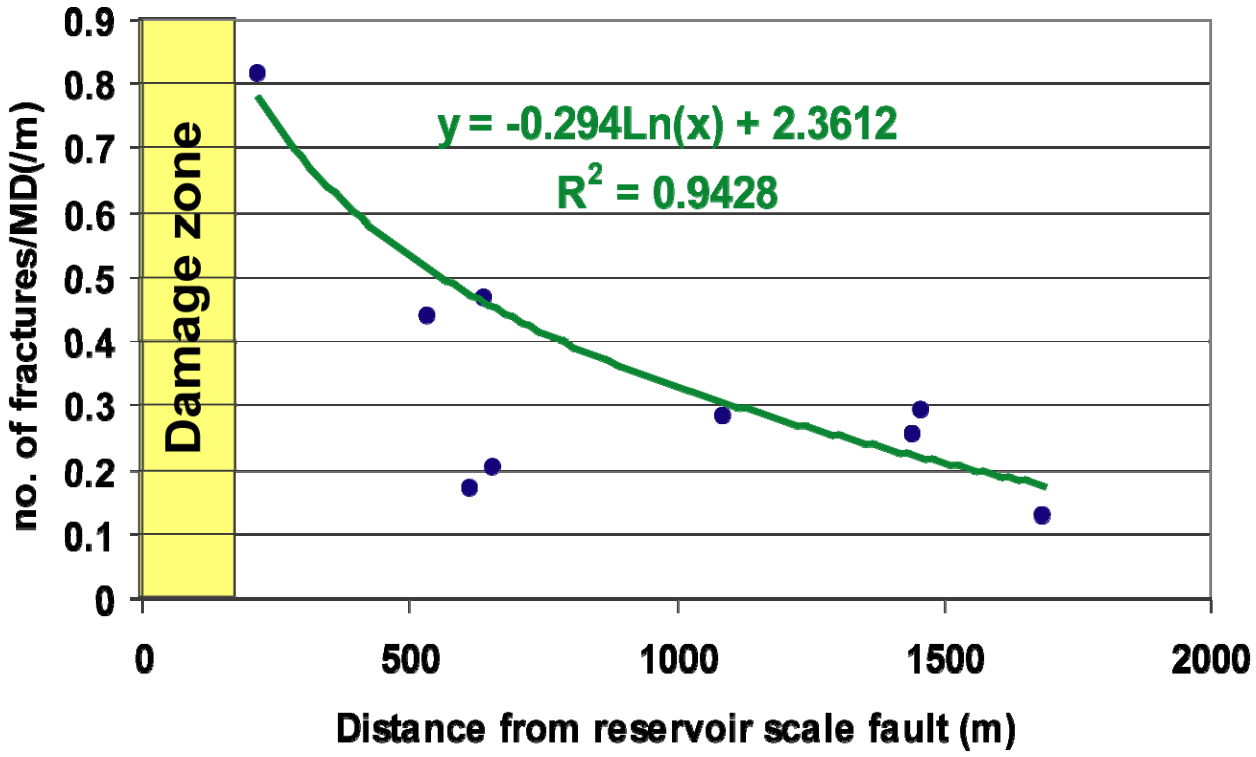

Fig. 10: Observed data at well locations indicate that fracture density decreases as a function of log of distance from the reservoir scale faults.

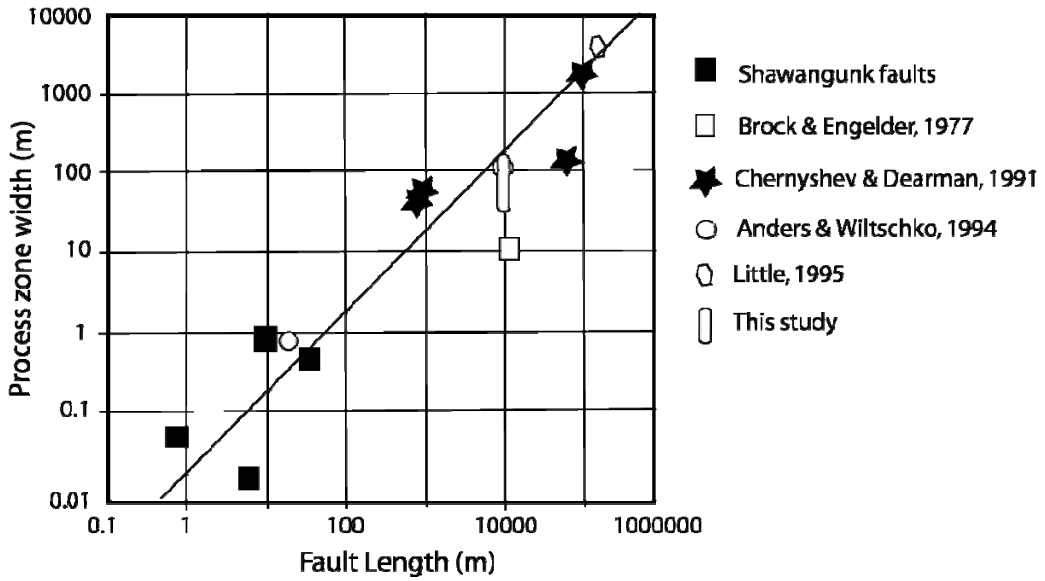

Fig. 11: The width of the process zone linearly scales to the length of the fault (modified from Vermilye and Scholz et al.[23]).

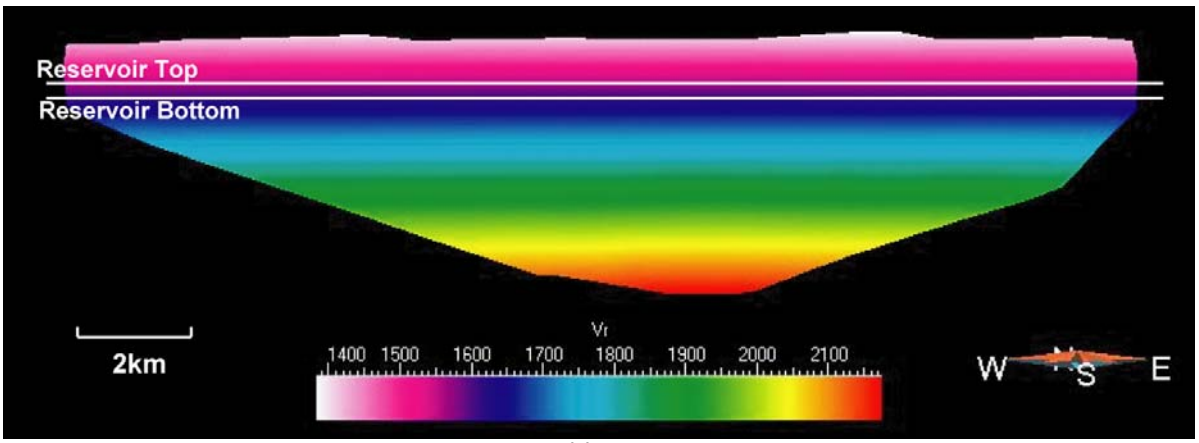

(a)

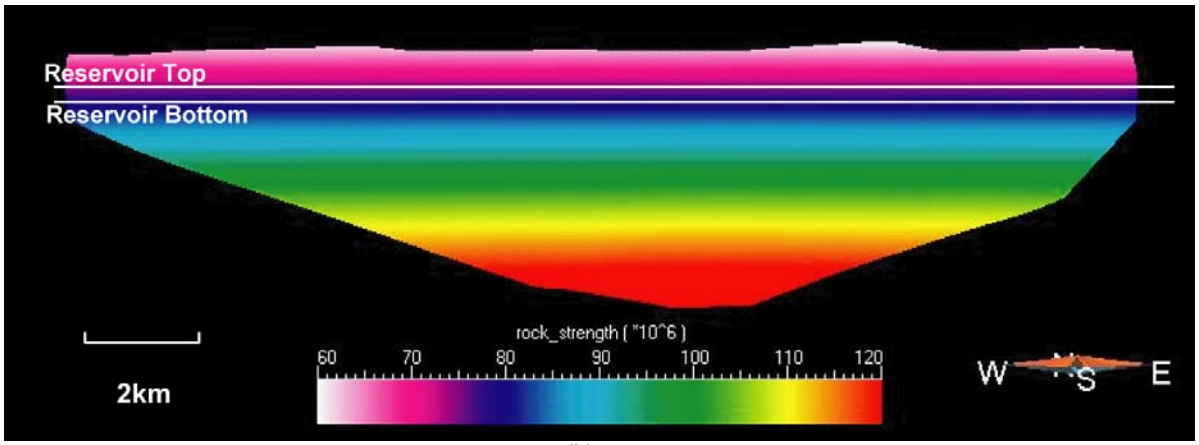

(b)

Fig. 12: (a) Rupture velocity (m/s), and (b) Rock strength (Pa) profiles along a reservoir scale fault. These profiles are calculated using confining pressure at a depth ~2/3 of the current depth to model the stress environment where we postulate that fault slip occurred.

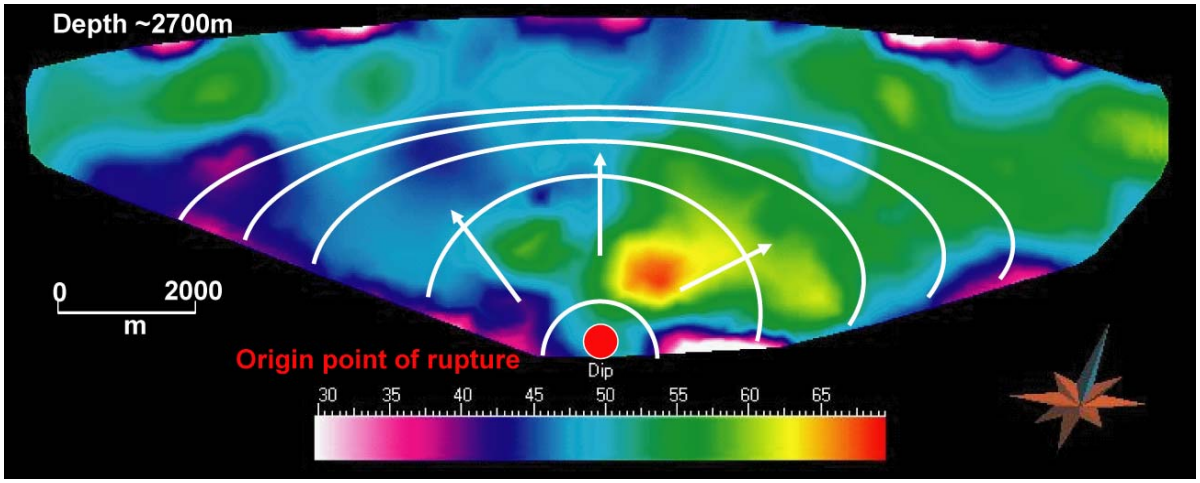

Fig. 13: Rupture is assumed to originate at the bottom-center of the fault The rupture zone initially has a circular pattern but gradually becomes elliptical. Color in the figure indicates dip on the fault plane.

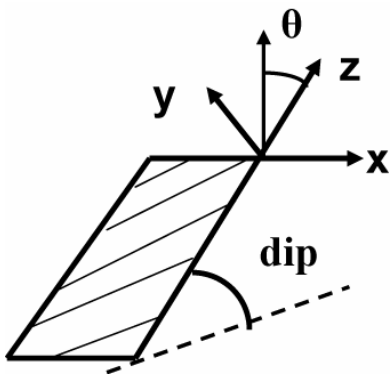

(a)

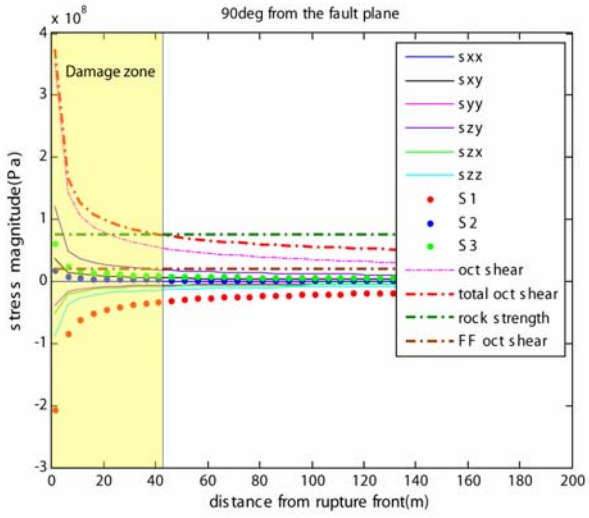

(b)

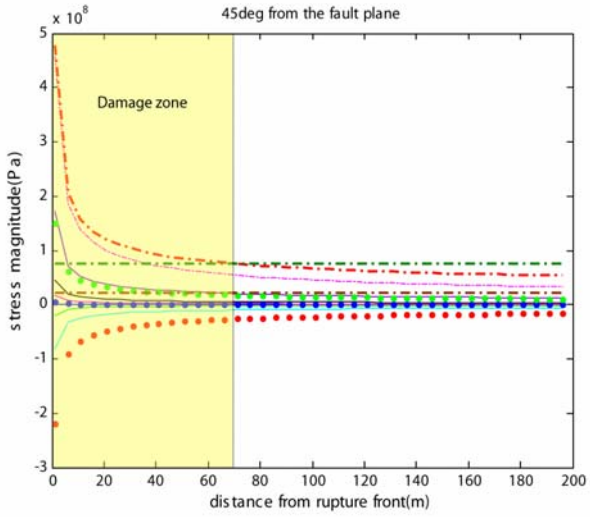

(c)

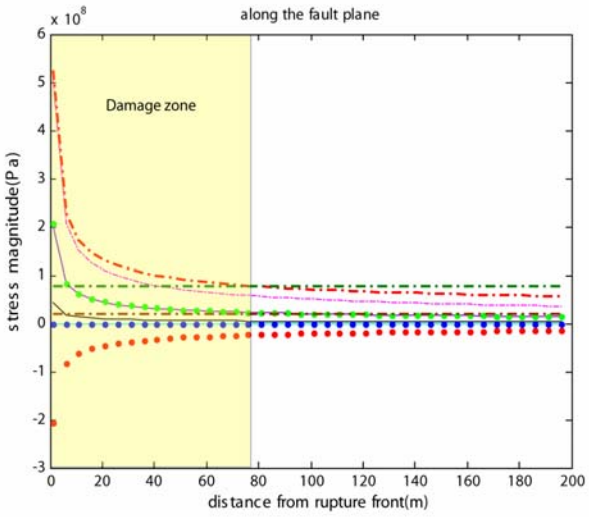

(d)

Fig. 14: (a) The coordinate system at the rupture front. In (b) 90º, (c) 45º, and (d) 0º direction, we see stress tensor, principal stresses, octahedral shear stress due to dynamic rupture propagation, far-field octahedral shear stress, total octahedral shear stress, and rock strength at the rupture front. The damage zone is created when total octahedral shear stress is greater than rock strength.

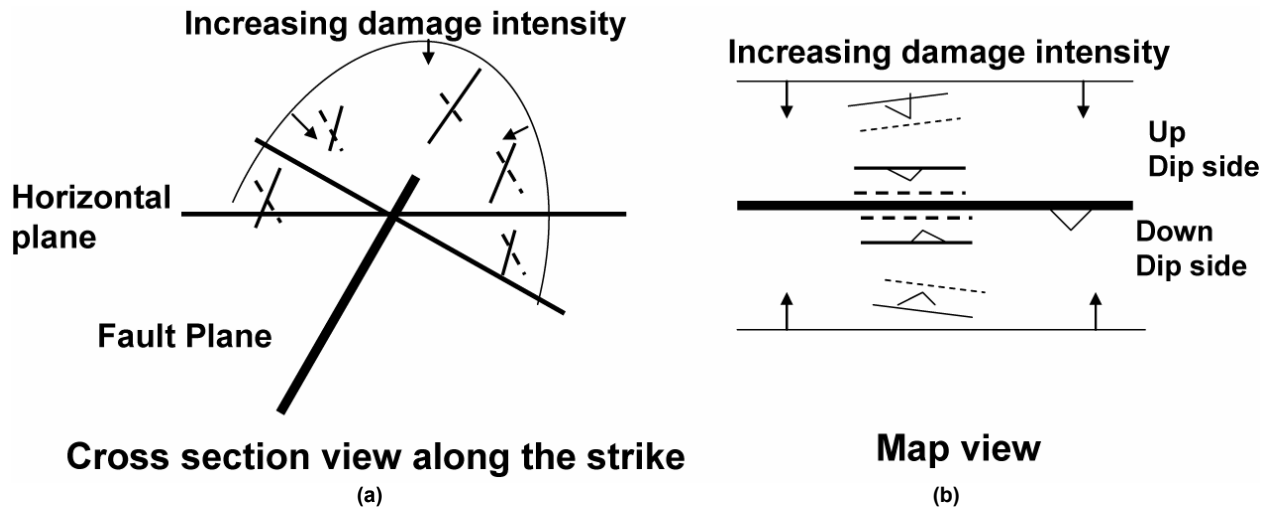

Fig. 15: (a) Cross section view of the damage zone along the strike, and (b) Map view of the damage zone. Away from the fault plane (90º) failure planes are at higher angle than along the fault plane (0º) and damage intensity increases as we get close to the fault.

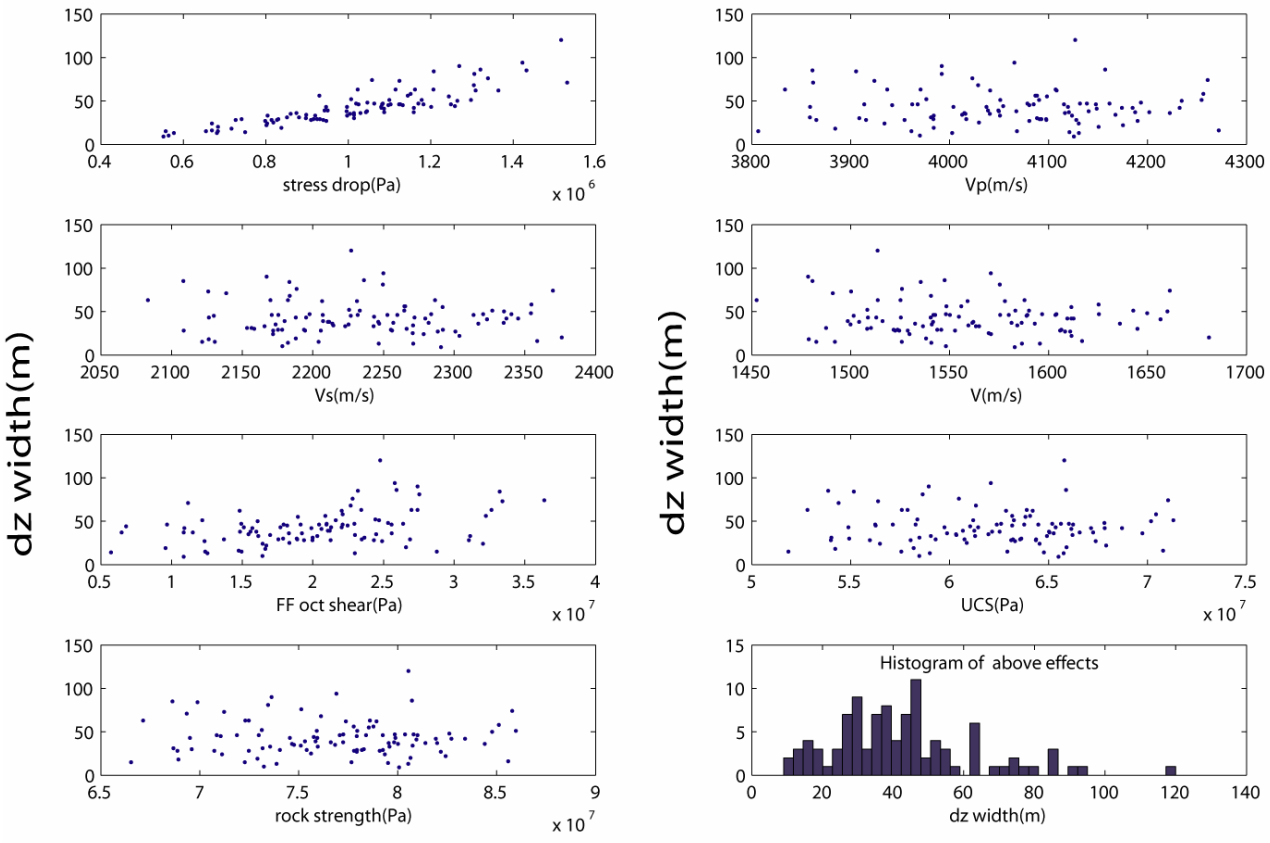

Fig. 16: The damage zone modeling is most sensitive to the stress drop among all the input parameters. The histogram of damage zone width shows the dominant uncertainty range is between 20m to 60m with an average ~45m.

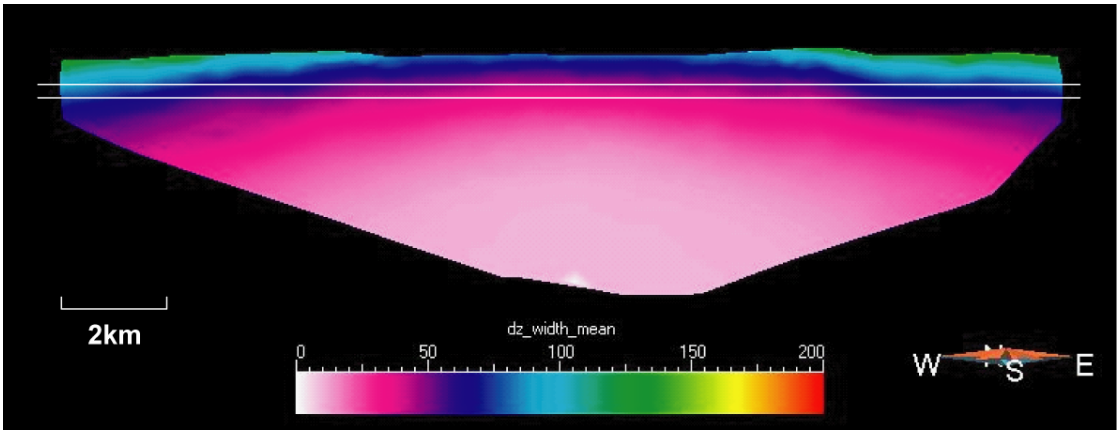

(a)

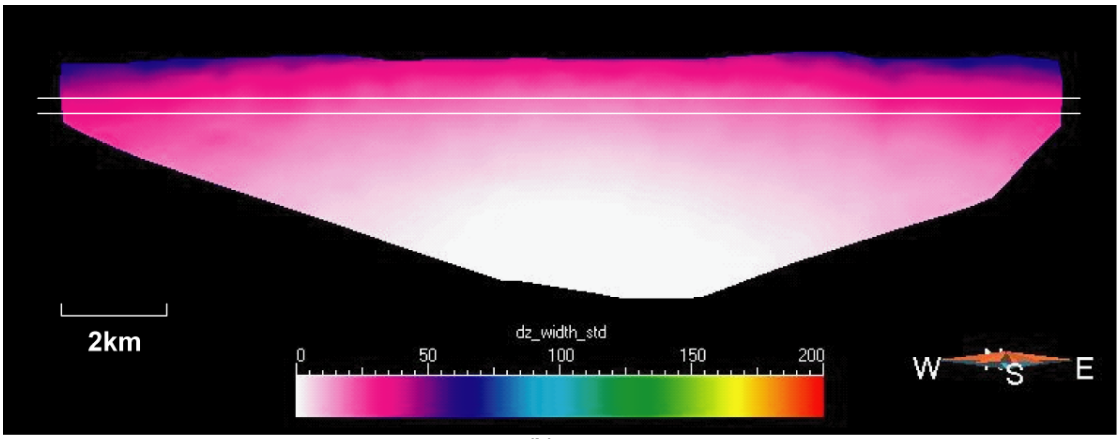

(b)

Fig. 17: (a) The mean and (b) the standard deviation of the damage zone width (m) from 100 simulations. The average damage zone at the reservoir depth varies from ~40m at the center to ~80m at edges. Standard deviation increases with the increase in the damage zone width.

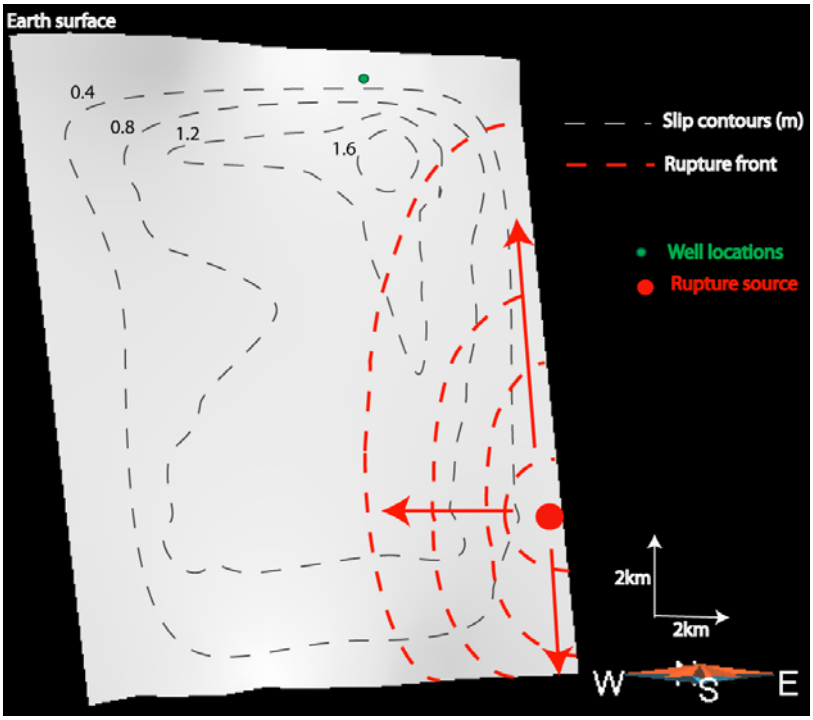

Fig. 18: A cross sectional view of the Nojima fault from the south. Gray dashed lines indicate slip on the fault due to Kobe 1995 earthquake, estimated by combined source inversion technique[44]. Red dot is the hypocenter or rupture source point of the earthquake, which is located ~17km beneath the surface at the north edge of the fault.

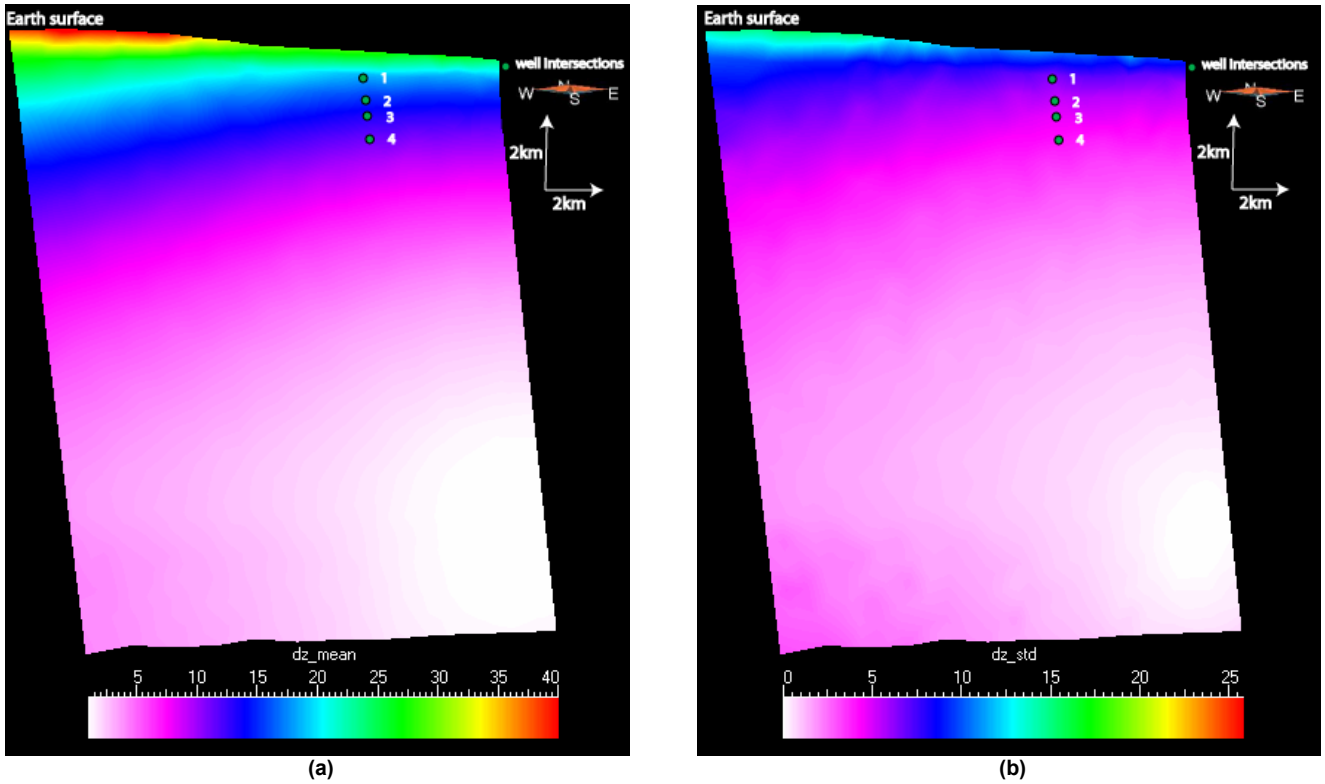

Fig. 19: (a) Mean damage zone width and (b) standard deviation of the width in meters along the Nojima fault. Well intersections points are shown as 1,2,3, and 4. The damage zone width decreases with increase in depth.

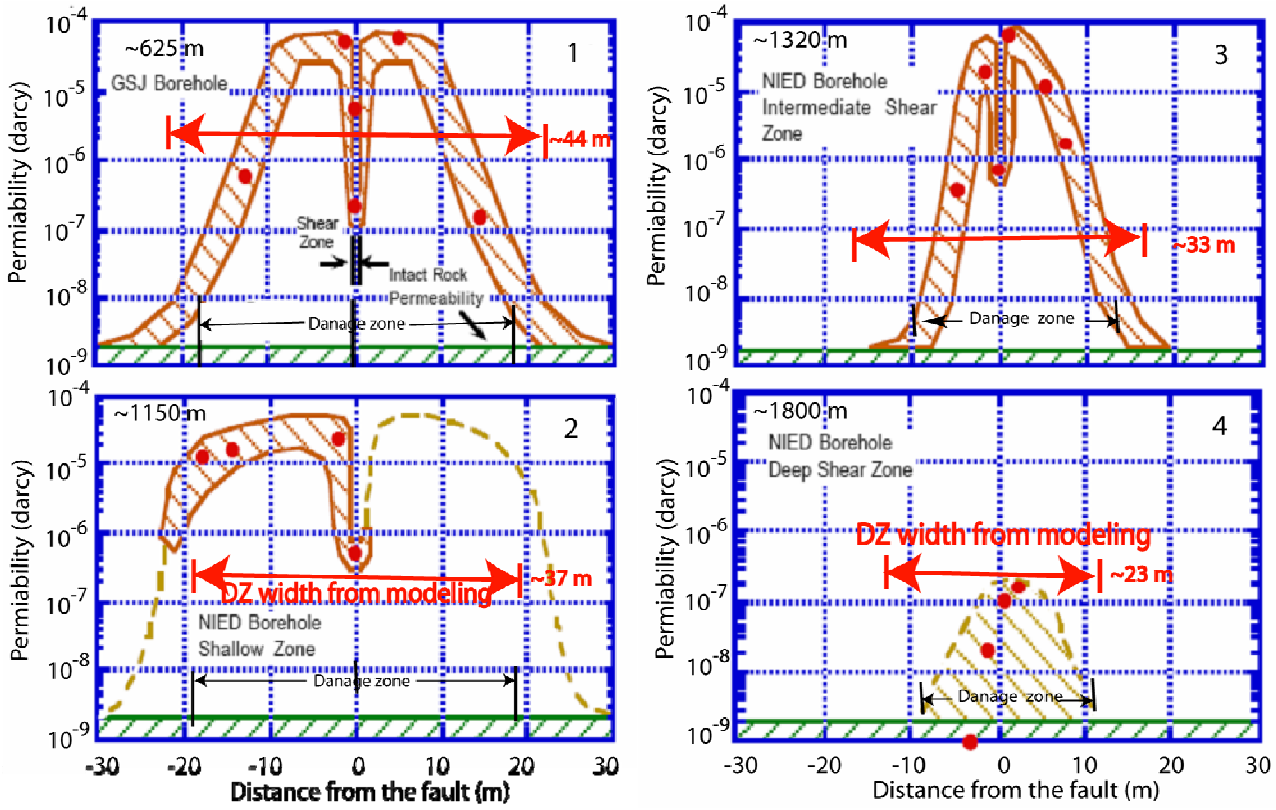

Fig. 20: The damage zone widths estimated using the rupture propagation technique (shown in red lines) are consistent with the damage zone width observed in GSJ and NIED boreholes. Matrix permeability measured at 50 MPa effective confining pressure indicate 4-5 order magnitude higher permeability in comparison to the intact rock permeability.[46]

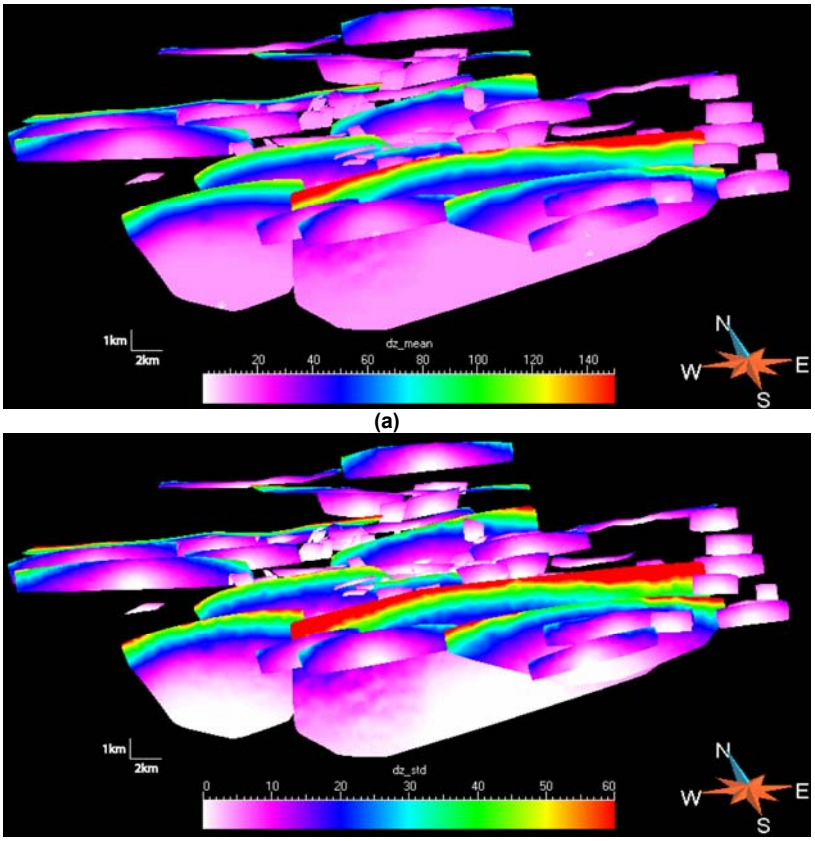

Fig. 21: (a) Mean damage zone width and (b) standard deviation of the width in meters along the EW trending fault of the CS field (south view).

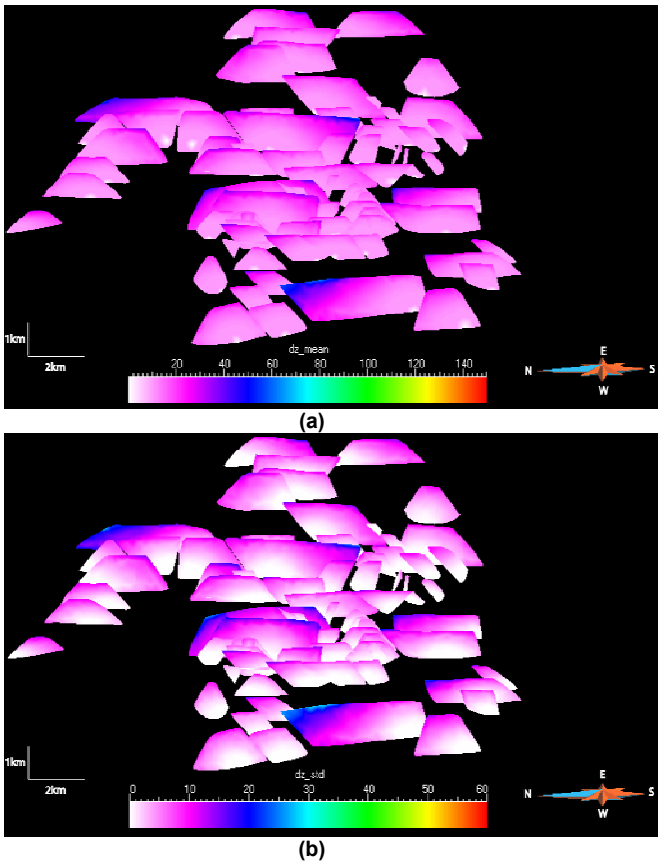

Fig. 22: (a) Mean damage zone width and (b) standard deviation of the width in meters along the NS trending fault of the CS field (west view).

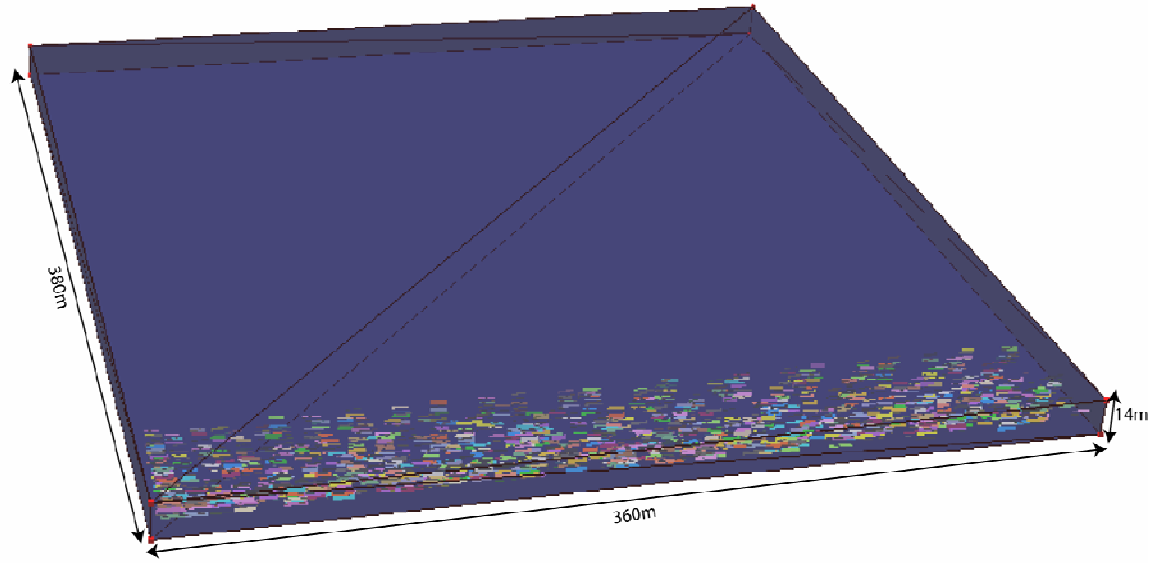

Fig. 23: Discrete fractures associated with the fault damage zone within one grid block. Grid size represents the average grid block size of the upscaled model of the CS field.

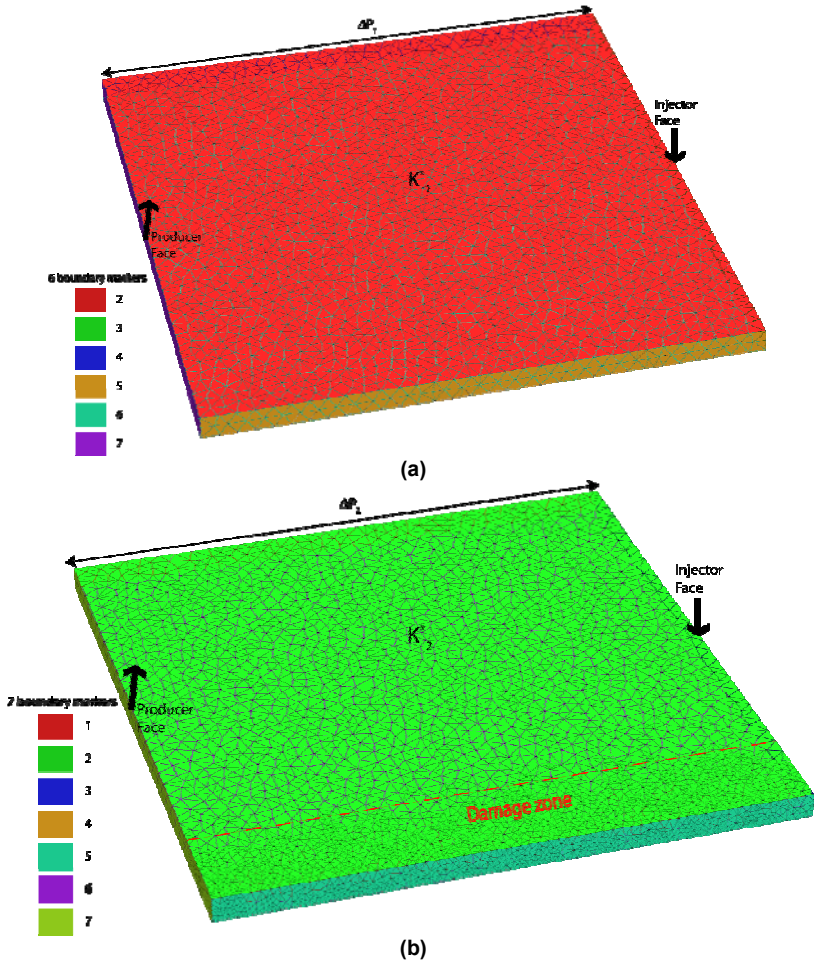

Fig. 24: The fine scale unstructured grid of one grid block (a) without damage zone and (b) with damage zone (damage zone is represented as very fine grid cells). In a steady state with similar injection and production constraints, the ratio of pressure difference between injection and production face gives the change in permeability along the flow direction.